Quasi-steady circulation regimes in the Baltic Sea

1

2 **Taavi Liblik[1], Germo Väli[1], Kai Salm[1], Jaan Laanemets[1], Madis-Jaak Lilover[1], Urmas Lips[1]**

3

4 [1]Department of Marine Systems, Tallinn University of Technology, Tallinn, Estonia

5 *** Correspondence:**
6 Taavi Liblik
7 taavi.liblik@taltech.ee

10 **Abstract.** Circulation plays an essential role in the creation of physical and biogeochemical fluxes in
11 the Baltic Sea. The main aim of the work was to study the quasi-steady circulation patterns under
12 prevailing forcing conditions.

13 Six months of continuous vertical profiling and fixed-point measurements of currents, two monthly
14 underwater glider surveys, and numerical modeling were applied in the central Baltic Sea. The vertical
15 structure of currents was strongly linked to the location of the two pycnoclines: the seasonal
16 thermocline and the halocline. The vertical movements of pycnoclines and velocity shear maxima were
17 synchronous. The quasi-steady circulation patterns were in geostrophic balance and high-persistent.
18 The persistent patterns included circulation features such as upwelling, downwelling, boundary
19 current, and sub-halocline gravity current. The patterns had a prevailing zonal scale of 5–60 km and
20 considerably higher magnitude and different direction than the long-term mean circulation pattern.

21 Northward (southward) geostrophic boundary current in the upper layer was observed along the eastern
22 coast of the central Baltic in the case of southwesterly (northerly) wind. The geostrophic current at the
23 boundary was often a consequence of wind-driven, across-shore advection.

24 The sub-halocline quasi-permanent gravity current with a width of 10–30 km from the Gotland Deep
25 to the north over the narrow sill separating the Farö Deep and Northern Deep was detected in the
26 simulation, and it was confirmed by an Argo float trajectory. According to the simulation, a strong
27 flow, mostly to the north, with a zonal scale of 5 km occurred at the sill. This current is an important
28 deeper limb of the overturning circulation of the Baltic Sea. The current was~~is~~ stronger with northerly
29 winds and restricted by the southwesterly winds.

30 The circulation regime ha~~s~~d an annual cycle due to seasonality in the forcing. Boundary current~~s~~ was~~are~~
31 stronger and more frequent~~ly~~ northward during the winter period. The sub-halocline current towards
32 the north was~~is~~ strongest in March–May and weakest in November–December.

33

34

1   Introduction

Current structure is an important player in the physical and biogeochemical fluxes in ocean. The semi-enclosed, shallow, brackish Baltic Sea has a strong but variable vertical stratification characterized by two pycnoclines: the permanent halocline and the seasonal thermocline (Leppäranta & Myrberg, 2009). Three-layer structure occurs in summer and consists of warm and fresh upper mixed layer, cold and saltier intermediate layer, and warmer and saltiest deep layer. Water column is mixed up to the permanent halocline at 60–80 m depth and cold intermediate water forms during winters. Stratification through the two pycnoclines impedes vertical mixing, and transport of substances between the layers is limited. The role of tides is marginal in the Baltic Sea. Lateral flows play an important role in distributing the water properties.

Water-mass circulation of the Baltic Sea is determined by the saline water inflow from the North Sea and freshwater input from the catchment area. The interaction of the fresher and saltier waters forms the so-called Baltic haline conveyor belt (Döös et al., 2004). The belt consists of saltier water transport and signal propagation in the deep layer towards the north-eastern end of the Baltic (Liblik et al., 2018; Väli et al., 2013); upward salt flux through vertical mixing and transport (Reissmann et al., 2009), and outflow of the mix of riverine and saltier water in the upper layer (Jakobsen et al., 2010). The conveyor determines salinity, stratification and other important characteristics for the pelagic ecosystem.

The largest basin in the sea, the Baltic Proper (Fig. 1a) is a source for the deep waters of the Gulf of Riga, Gulf of Finland and Gulf of Bothnia. Permanent oxygen depletion has expanded in recent decades in the Baltic Sea, forming one of the largest dead zones in the global ocean (e.g. Carstensen et al., 2014). Only Major Baltic Inflows (Matthäus & Franck, 1992; Mohrholz, 2018) ventilate the deep layers of the southern and central Baltic Proper (Holtermann et al., 2017) but increase hypoxia in the Northern Baltic Proper and Gulf of Finland (Liblik et al., 2018) due to transport of former anoxic/hyppoxic Eastern Gotland Basin water and stronger stratification (Liblik et al., 2018).

The basin-scale pattern of the long-term mean circulation in the Baltic Proper is cyclonic as demonstrated by several modeling studies (Hinrichsen et al., 2018; Jedrasik et al., 2008; Jędrasik & Kowalewski, 2019; Meier, 2007; Placke et al., 2018). The mean circulation is to the north along the eastern coast of the Baltic Proper and to the south along the eastern and western coast of Gotland Island (Meier, 2007; Placke et al., 2018). The turning area for this basin-wide cyclonic circulation cell in the north is between 59 to 59.5° N (Meier, 2007). The zonal center of the cyclonic flow in the Eastern Gotland Basin is in the Gotland Deep (Placke et al., 2018). The cyclonic structure exists from the bottom to the surface (Placke et al., 2018), although lateral structure and magnitude of the flow vary among different models (Placke et al., 2018). It is important to note that all aforementioned descriptors of the long-term mean flow rely on numerical simulations and lack support from observations. However, a consistent northward low-frequency current along the eastern slope of the Gotland Deep at 204 m depth has been reported (Hagen & Feistel, 2004). Placke et al. (2018) compared simulated currents with these measurements. All model simulations showed the mean meridional northward current velocity in the range of 0–1 cm s^{-1} (actually, three models out of four had values of 0.0–0.1 cm s^{-1}) while the measurements gave the mean northward velocity of 3 cm s^{-1} (Hagen & Feistel, 2004). Thus, the long-term mean flow to north in the deep layer was much stronger than the simulated mean current.

77 Temporal variability of currents in the Baltic Sea is very high as a reaction to atmospheric forcing.
78 Near-shore Eulerian current observations (Sokolov & Chubarenko, 2012) and drifter experiments
79 (Golenko et al., 2017; Krayushkin et al., 2019) conducted in the southern Baltic Proper showed a strong
80 correlation between wind and surface currents. Current velocity spectra in the Baltic include seiches
81 and tides with different periods from 11 h to 31 h and inertial motions with a period of about 14 h
82 (Jönsson et al., 2008; Lilover et al., 2011; Suhhova et al., 2018).

83 The vertical current structure through thermocline and halocline has not been rigorously studied by the
84 in-situ observations in the Baltic Proper. Moreover, despite a considerable effort to reveal the spatial,
85 long-term mean circulation patterns based on the simulations, not much has been done to study
86 temporal developments of currents in the synoptic (mesoscale) and seasonal timescales in the Baltic
87 Proper. In the present work, we address this shortage of knowledge.

88 Permanent circulation systems, such as boundary currents or subtropical gyres, are key processes that
89 determine transport in the open ocean (e.g. Macdonald, 1998). Although there are no permanent
90 currents in the Baltic Sea, we hypothesize that under stable wind forcing and stratification conditions,
91 a steady circulation regime prevails in the time-scale of days to weeks and has a much greater
92 magnitude than the mean current structures. These quasi-steady circulation features could be related to
93 the downwelling and upwelling processes or appear as a boundary current or a gravity current under
94 the halocline.

95 Following a description of the methods used, we present an analysis of (1) boundary current under
96 variable wind forcing and stratification, (2) quasi-permanent circulation patterns, and (3) sub-halocline
97 current. The analysis of observational and simulation results is followed by discussion and conclusions.
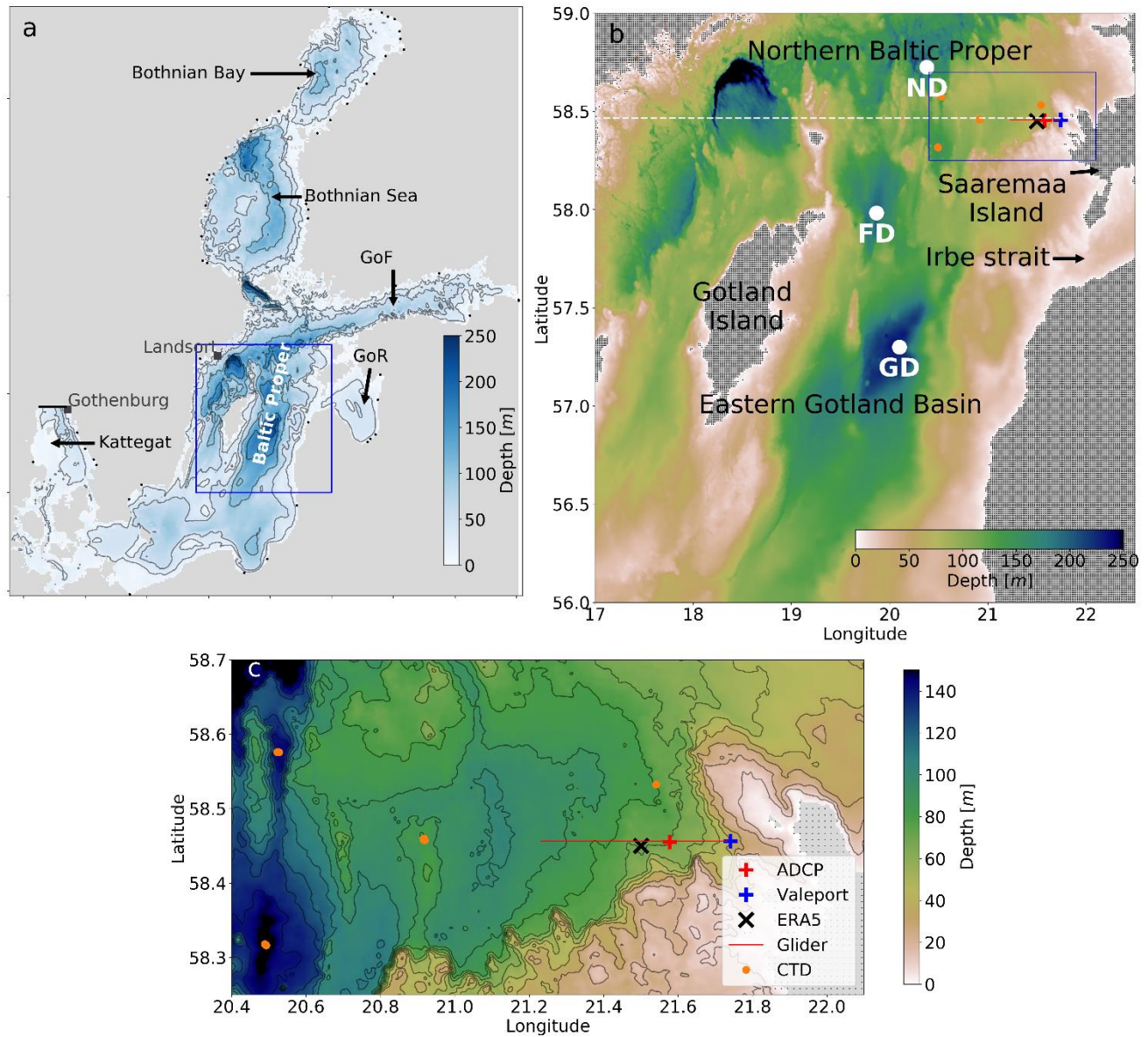
Figure 1. (a) Map of the Baltic sea and model domain. Shown are the locations of the open boundary of the model domain in the Kattegat (bold black line), Landsort and Gothenburg sea level stations, Baltic Sea rivers used in the model (black dots) and study area (~~black~~ blue box). (b) Close-up of the study area. Locations of ADCP and Valeport moorings, CTD measurements, glider section, the center of the cell of ERA5 wind data, and zonal section along the latitude of the ADCP location in the Nortern Baltic Proper (white dashed line) are presented. Gotland Deep (GD), Fårö Deep (FD) and Northern Deep (ND) are also shown. (c) Close view of the moorings and CTD measurement locations, glider section, and local topography are shown. Dots on land (b, c) illustrate the model grid.

2   Data and methods

2.1 Observations and data products

A bottom mounted current profiler ADCP 300 kHz (Teledyne RDI) and model 106 current meter (Valeport Ltd) (hereinafter referred to as Valeport) were deployed at the end of February to the west

112   of Saaremaa Island (Fig. 1b and c). Valeport was mounted at 5 m depth, while the sea bottom depth in
113   its location (58° 27.4' N, 21° 44.4' E) was 41 m. The sea depth in the ADCP location (58° 27.3' N, 21°
114   34.6' E) was 71 m and velocities were measured with vertical depth interval of 2 m in the depth range
115   of 10–68 m. Current velocity profiles were recorded as average of 1 h. The quality of the current
116   velocity data was checked following the procedure developed by Book (et al., 2007). Valeport recorded
117   current velocity with 10 min intervals. A Seabird SBE 16*Plus* V2 CTD SEACAT conductivity and
118   temperature recorder was deployed together with the ADCP, but it hung 4 m above the sea bottom, i.e.,
119   at a depth of 67 m. SBE 16*Plus* sensors were calibrated by the manufacturer before the deployment.

120   Repeated CTD profiles onboard R/V Salme were collected using an OS320 CTD probe (Idronaut S.r.l.)
121   in the Northern Baltic Proper (see Fig. 1b and c) from 30 January to 4 August 2020.

122   Argo float deployment was arranged by the Finnish Meteorological Institute (Siiriä et al., 2019) from
123   15 August 2013 to 15 August 2014 and the trajectory data was derived from the Argo-based deep
124   displacement dataset (Ollitrault & Rannou, 2013). The dataset was downloaded on 15 March 2021 at
125   https://www.seanoe.org/data/00360/47077/.

126   In 2020, two glider missions were conducted in the Northern Baltic Proper. The Slocum G2 Glider
127   collected oceanographic data along the E–W oriented 27 km long section (Fig. 1b and c). The
128   easternmost point of the glider track was approximately 7 km off the shoreline and the section was
129   located at the sloping bottom where sea depth gradually deepened westward from 40 m to 90 m. The
130   first mission was carried out from 28 February to 22 March 2020 and the second one from 4 August to
131   2 September 2020. Both ascending and descending profiles were recorded and altogether over 8000
132   profiles were gathered. The glider moved at a horizontal speed of 0.33 ± 0.08 m s^{-1}. On average, a profile
133   took 8.0 ± 0.9 min to complete 80–90 m deep profile and the average distance between the profiles near
134   the surface was 301 ± 46 m. Both the sampling time and the distance were decreased by half in the
135   shallow part of the section.

136   Preliminary glider data processing included the standard quality control (impossible date and location
137   test, range tests for the sensors; practically no incorrect data were detected) and accounting for the
138   response time of the sensors and the thermal lag. First, a linear time shift was applied to temperature
139   and conductivity considering the misalignment with pressure. Temperature was re-aligned by 1.4 s and
140   conductivity by 0.9 s for the mission conducted in the spring and respectively by 1.6 s and 1.1 s for the
141   mission in the summer. The parameters were chosen by comparing consecutive profiles focusing on
142   the depth range around the greatest gradient. It was assumed that successive profiles correspond to the
143   same water mass. We followed Mensah et al. (2009) to remove the thermal lag effect and found optimal
144   coefficients for the temperature error amplitude, α, and time constant, t_c, by comparing consecutive
145   TS-profiles. The satisfying results were obtained in the case of $\alpha = 0.0025$ and $t_c = 10$ s for the earlier
146   mission and $\alpha = 0.055$ and $t_c = 12$ s for the following one. The profiles were averaged on a 0.5 dbar
147   vertical grid after processing the raw data.

148

149   Sea surface temperature was derived from the Copernicus Marine Service product
150   SST_BAL_SST_L4_REP_OBSERVATIONS_010_016 with a horizontal resolution of 0.02 x 0.02
151   degrees. Mean difference between the product and in-situ data sources has been in the range of –0.12
152   to –0.21 °C and root mean square error from 0.43 to 0.88 °C depending on the data sources according
153   to the quality information document

154 (https://catalogue.marine.copernicus.eu/documents/QUID/CMEMS-SST-QUID-010-016.pdf,
155 accessed 19 August 2021).

156 Hourly, 10 m level wind velocities of ERA5 reanalysis data (Hersbach et al., 2020) at the cell with the
157 size 0.25°x0.25° from 1979 to 2020 (see Fig. 1 for location) were used in the analyses.

158

2.2 Modeling

160 Numerical model GETM (General Estuarine Transport Model, Burchard & Bolding, 2002) has been
161 applied to simulate the circulation and temperature/salinity distribution in the northeastern Baltic Sea.
162 GETM is a primitive equation, three-dimensional model with free surface and k–ε turbulence model
163 for vertical mixing by coupling the hydrodynamic part with GOTM (General Ocean Turbulence Model,
164 Umlauf & Burchard, 2005).

165 Model domain covered the whole Baltic Sea with the open boundary situated in the Kattegat region
166 (Fig. 1a). The horizontal grid spacing of the model was 0.5 nautical miles (926 m) and 60 vertically
167 adaptive coordinates (Hofmeister et al., 2010; Gräwe et al., 2015) were used. Sea surface height from
168 Gothenburg station has been used as the boundary condition to control the barotropic in- and outflow
169 from the Baltic Sea, while the temperature and salinity were nudged towards monthly climatological
170 profiles (Janssen et al., 1999) along the open boundary.

171 Data from the Estonian version of the operational model HIRLAM (High Resolution Limited Area
172 Model) maintained by the Estonian Weather Service and giving forecasts with hourly resolution
173 (Männik and Merilain, 2007) were used to calculate the momentum and heat flux at the sea surface.
174 Climatological runoff of the Baltic Sea rivers with inter-annual variability added from the values
175 reported to the HELCOM (Johansson, 2016) was used. Simulation covered period from April 2010 to
176 September 2020, and initial temperature and salinity fields were taken from the CMEMS (Copernicus
177 Marine Service) re-analysis product for the Baltic Sea.

178 The same setup of the model was previously used in Zhurbas et al. (2018) and Liblik et al. (2020) and
179 more details about the model setup are given there. Zhurbas et al. (2018) validated the salinity and
180 temperature values in the central Baltic Sea along with the sea surface height at Landsort station and
181 compared the near-bottom current statistics with the long-term observations in the Gotland Deep.
182 Liblik et al. (2020) validated the simulated wintertime sea surface temperature and salinity in the Gulf
183 of Finland and compared the observed mixed layer depth with the simulations. In this study, we will
184 present the comparison of simulated and observed currents in the Northern Baltic Proper.

185

2.3 Calculations

187 Isohaline 9 g kg^{-1} was selected to define the center of the halocline (CH) depth since the halocline was
188 steepest around this salinity value according to the salinity profiles. Isoterm 13 °C was selected to
189 define the center of the thermocline depth using the same logic. Thermocline was defined only for the
190 second glider mission in August 2020. To estimate the center of halocline depth based on single level
191 salinity time-series measured by the SBE 16*Plus*, and twelve CTD profiles collected by the RV Salme
192 in the Northern Baltic Proper (see Fig. 1b) from 30 January to 4 August 2020 were used. Salinity
193 profiles were vertically normalized by subtracting the depth of the CH at each profile. Next, the mean

194 salinity profile in the normalized depth coordinates was calculated (Fig. 2). The mean normalized depth
195 and salinity relationship were used to derive the CH depth from the SBE 16*Plus* salinity time-series at
196 67 m depth. If salinity was lower (higher) than 9 g kg^{-1}, the CH was deeper (shallower) than 67 m
197 according to the mean depth-salinity curve (Fig. 2). Maximum depth of the neighboring sea area, 88
198 m, was defined as the maximum depth of the CH.

199 In this study the *x*-axis is positive eastward, the *y*-axis is positive northward, and the *z*-axis is positive
200 upward (*z*=0 at the sea surface), *u* and *v* are horizontal velocity components.

201 The baroclinic components of the geostrophic velocity (*u_g and v_g*) can be deduced from the
202 hydrographic data. Considering the dynamic method, the geostrophic relationships are as follows

203 $v_g = \frac{1}{f}\frac{\partial \Phi}{\partial x}$

204 $u_g = -\frac{1}{f}\frac{\partial \Phi}{\partial y}$

205 The geopotential, Φ, is proportional to the dynamic height, D, as

206 $\Phi = gD$

207 where *g* is the gravitational acceleration and *f* is the Coriolis parameter.

208 The dynamic height can be determined from the temperature and salinity (density) profiles.

209 The relative geostrophic velocity was evaluated using dynamic height anomaly relative to a reference
210 pressure (McDougall & Barker, 2011). The geopotential slope of an isobaric surface expresses the
211 horizontal pressure gradient. A zonal glider track enabled to calculate the meridional velocity profile
212 of the geostrophic flow. The meridional geostrophic velocity was calculated also from the GETM
213 simulation data. The reference level was set at 70 dbar. The shallower profiles were included using the
214 stepped no-motion level method described in Rubio et al. (2009). Since velocity is not zero at the 70
215 dbar level, the calculated geostrophic velocities $V_{GEO-DENS-glider}$ and $V_{GEO-DENS-GETM}$ described in
216 subchapter 3.1 represent relative velocities to the no-motion 70 dbar level. Both variables represent an
217 averaged velocity at an extent of 10 km zonal scale around ADCP position.

218 To compare the simulated geostrophic velocity profiles with the measured ADCP velocity profiles, the
219 relative geostrophic velocity at the sea surface (calculated relative to 70 dbar using simulated density
220 profiles) was aligned with the geostrophic velocity due to the sea level gradient from the model
221 simulation ($V_{GEO-SL-GETM}$). Sea level gradient was estimated from linear regression fit of sea level
222 anomalies at a horizontal scale of 10 km. The difference (vector) between the density-estimated and
223 the sea level estimated geostrophic velocity at the sea surface was applied to the whole geostrophic
224 velocity profile under the assumption that the geostrophic current at the surface is determined by the
225 differences in the sea level exclusively. Adjusted geostrophic velocity profiles were presented as $V_{GEO-ADJ-GETM}$
226 $_{ADJ-GETM}$ in subchapter 3.2.
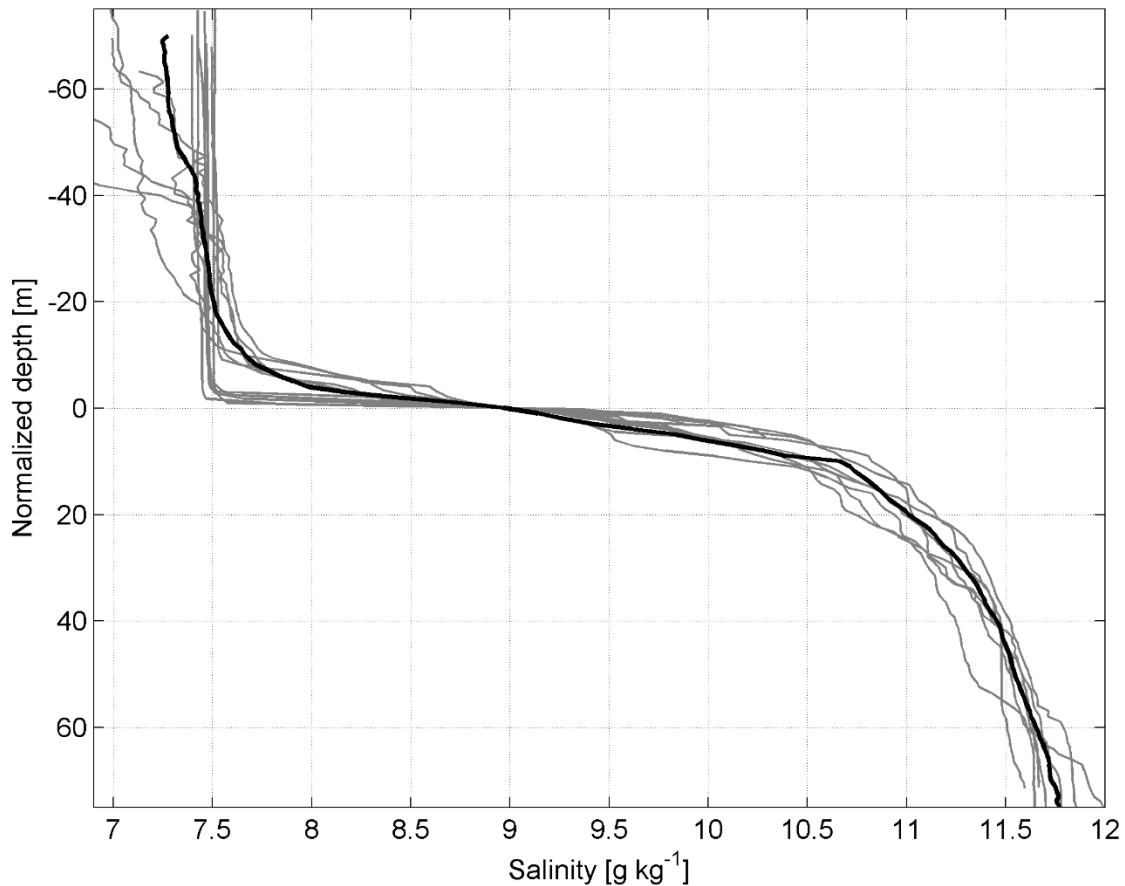
Figure 2. Vertically normalized salinity profiles from 30 January to 4 August 2020 in the Northern Baltic Proper (see Fig. 1b). Bold black line represents the mean salinity profile.

The direct influence of wind forcing on the subsurface currents was ascertained using the classical Ekman model based on the balance of the frictional and Coriolis forces (Ekman, 1905). Wind stress vector τ as the Ekman model input parameter was calculated using ERA5 (Fig. 1b and c) wind data: $\tau = \rho_{air} cd |\mathbf{U}| \mathbf{U}$, which were prior low-pass filtered with cut-off 36 hours to exclude periodic processes. Here $\mathbf{U}$ is the wind velocity vector at 10 m height, cd is the drag coefficient and was parameterized as proposed by (Wu, 1980): $cd = (0.8 + 0.065|\mathbf{U}|) \times 10^{-3}$, $|\mathbf{U}|$ is the wind velocity vector module and ρ_{air} is the density of air. The eddy viscosity used in the model was calculated according to (Csanady, 1981): $v = |\tau|/200f$, where $|\tau|$ is the wind stress vector module. The model outputs are the vertical profiles of wind-induced current velocity components.

The temporal development in the vertical current structure is presented as the time-series of vertical current shear squared $s^2 = (\partial u/\partial z)^2 + (\partial v/\partial z)^2$.

Persistency of the current, characterizing the variability of the direction of the flow, is defined as the ratio between vector and scalar current speeds:

8

243 $$R = \frac{\sqrt{u^2+v^2}}{\frac{1}{N}\Sigma\sqrt{u_n^2+v_n^2}}.$$ Current and wind

244 velocity components are presented as 36-h and 10-day low-passed time-series. The fourth-order
245 Butterworth filter was used for low-pass filtering.

3 Results

3.1 Boundary current under variable wind forcing

248 Statistics of the 6 months (1 March–1 September 2020) ADCP current data~~deployment~~ revealed the
249 persistency of currents between 32 and 42%, with the highest persistency in the 20–40 m depth range
250 (Table 1). Mean and maximum hourly measured speeds were higher in the uppermost bin at 11 m
251 depth, 11 and 48 cm s^{-1}, respectively and lower in the near-bottom layer, 7 and 34 cm s^{-1}. The mean
252 u- and v-components were positive in all depths showing the mean flow to the NE sector.

253 From the flow structure point of view the ADCP current velocity time series can be divided into two
254 periods: 1) from March until mid-April, when barotropic regime prevailed, 2) from mid-April until
255 September, when layered flow dominated (Fig. 3a and b). One can also see the coincidence of the
256 current u- and v-components in the uppermost and deepest bin during the first period (Fig. 3c and d)
257 except a short period at the end of March. Discrepancies between the two layers afterwards illustrated
258 the layered, baroclinic nature of the flow. The flow regime reacted well to wind forcing. Barotropic
259 flow to the northeast prevailed as a result of southwesterly winds until mid-April (Fig. 4). Only during
260 the last week of March, when wind was from northerly directions, a strong southerly current was
261 observed. Similar temporal patterns appeared in the upper layer in the stratified period. Alteration of
262 positive and negative meridional velocities was related to the prevailing wind direction. These
263 tendencies were evident both in the ADCP and Valeport locations. Deep layer current was directed to
264 the east, i.e., onshore, when southerly flow occurred in the upper layer and to the west or southwest,
265 when the current to the northeast prevailed. These are signs of the layered structure of the coastal
266 upwelling and downwelling.

267 The most frequent current direction in the upper layer (at a depth of 11 m ~~depth~~) was 40° at the ADCP
268 location. To estimate the relationship between the low-frequency (10-day low-passed) current
269 component and wind, we calculated the correlation between the 40° current velocity component (c_{40})
270 in the upper layer and wind speed from different directions with different time lags. The best correlation
271 ($r^2=0.65$, $p<10^{-100}$, n=4473) was found with the wind from the south, specifically towards 10° (w_{10}),
272 applying a 3-day time lag. This, on the one hand, corresponds to Ekman's theory, however, on the
273 other hand, the 3-day delay is rather long. Probably it can be explained by the mixed effect of wind on
274 the surface currents. The momentum flux created by wind impacts the current field fast. The correlation
275 without delay is relatively high ($r^2=0.55$, $p<10^{-100}$, n=4473) as well. The flow resulting from the sea
276 level gradient and due to the inclination of isopycnal surfaces are also a consequence of wind but
277 develop slower.

278 Time series of c_{40} reveal negative values from mid-April until the end of June (Fig. 3e). Before mid-
279 March and in July–August, the c_{40} was mostly positive. The main course of w_{10} and c_{40} coincided well,
280 but discrepancies occurred in the details. For instance, negative c_{40} occurred when w_{10} was positive in
281 the ADCP location in the last third of March and first half of May. The mean values of w_{10} and c_{40}
282 during the measurements were 0.6 m s^{-1} and 3.2 cm s^{-1}, respectively. The w_{10} is higher in winter and
283 smaller in summer. C~~C~~onsidering the linear relation between the two variables, the 1979–2020 mean
284 $w_{10} = 1.1$ m s^{-1} corresponds to $c_{40} = 4.2$ cm s^{-1}.

285 ~~The most frequent current direction was 350° at~~ At the Valeport location, the most frequent current
286 direction was 350°. The discrepancy between the dominant flow direction at the ADCP and Valeport
287 locations is related to the topographic features (Fig. 1). However, from the wider Baltic Sea dynamics
288 point of view the meridional current component is important to investigate. To study the temporal
289 developments of the meridional current, we next analyze the measured and simulated meridional
290 current components at 11 m depth at the ADCP location, V_{ADCP} and V_{GETM}. We also calculated the
291 geostrophic meridional component $V_{GEO-SL-GETM}$ of the current velocity from the simulated sea level
292 gradient and~~,~~ relative geostrophic meridional current component ($V_{GEO-DENS-GETM}$) at 11 m depth based
293 on simulated temperature and salinity data in the section. The relative geostrophic meridional
294 component ($V_{GEO-DENS-glider}$) was calculated using ~~and same for~~ the glider temperature and salinity data
295 as well~~($V_{GEO-DENS-glider}$)~~. We also calculated mean Ekman current u- and v-components in the depth
296 range 0–10 m U_{Ekman} and V_{Ekman}, respectively. All parameters are 36-h low-pass~~ed~~ filtered.

297 Overall, the simulated V_{GETM} ~~reasonably well~~ follows the temporal changes in measured V_{ADCP}
298 reasonably well (Fig. 5). V_{GETM} tends to have smaller values than V_{ADCP}, which means that the
299 meridional component of simulated velocity is biased southward. Sometimes, e.g., in June and August,
300 the discrepancies are considerable. Geostrophic meridional current component $V_{GEO-DENS-GETM}$ was
301 very small, and $V_{GEO-DENS-glider}$ was practically zero in March (Fig. 5b) as the water column was mixed
302 down to the reference depth of the geostrophic current calculation. Since the end of March, overall
303 temporal developments in the meridional current components (V_{ADCP} and V_{GETM}) and its geostrophic
304 meridional components ($V_{GEO-DENS-GETM}$), ($V_{GEO-SL-GETM}$) and $V_{GEO-DENS-glider}$) in August match quite
305 well (Fig. 5a and b). This can be related to the multiple effects of wind. South-westerly wind resulted
306 in the Ekman current towards the eastern coast of the Northern Baltic Proper. This caused, first, a sea
307 level gradient across the basin (higher near the coast), which induced barotropic current to the north.
308 Secondly, it ~~evoked~~ induced downwelling along the coast and resulted in a vertical gradient of the
309 geostrophic current. Such events were detected at the beginning of April and July, when strong
310 southwesterly winds blew (Fig. 4) and caused Ekman current towards the coast (Fig. 5c). Northerly or
311 northeasterly winds caused opposite effects. Sea level was lower near the coast compared to offshore
312 and thermocline was located at shallower depths near the coast. Thus, the flow was directed to the
313 south in the surface layer. Such events occurred in late March and mid-August. Most of the major
314 events of the positive V_{ADCP} and V_{GETM} were associated with the positive u-component of the Ekman
315 current (cf. Fig. 5a and c), i.e., flow towards the shore, not along the shore. Thus, the wind-driven
316 strong coastal current to the north is not induced by the direct momentum flux created by wind stress
317 but rather is the result of wind-driven sea level gradient and depression of the pycnoclines at the coast,
318 which resulted in vertically sheared geostrophic current.

319 Next, we consider the relationship between the vertical maxima of the current shear and the vertical
320 location of pycnoclines – seasonal thermocline and halocline. Seasonal thermocline began to develop
321 from the beginning of May (Fig. 6a). The temporal course of salinity at 67 m depth (Fig. 6b) and depth
322 of halocline center (Fig. 6d) showed that halocline was mostly located deeper than the deepest ADCP
323 bin. At the end of March, the halocline center reached 55 m depth (Fig. 6d) and high current shear
324 values were observed below 45 m depth (Fig. 6c). Shallower halocline was related to the northerly
325 wind event (Fig. 4), which caused offshore Ekman transport in the upper layer and compensating
326 onshore flow in the deep layer (Fig. 3). Such events of high current shear in the deep layer also occurred
327 at the end of April to early May, from the end of May to mid-June and in mid-August (Fig. 6c) when
328 the halocline center was shallower, and salinity increased at 67 m depth. Note that the depth of the
329 halocline center and shear maxima were vertically shifted, halocline center was deeper. This can be
330 explained by the vertical range of the halocline. The upper boundary of the halocline is shallower than

the center of the halocline. Thus, the shear maxima were rather linked to the upper boundary of the halocline.

Stronger and more extensive shear maxima in the upper part of the water column were observed since late April (Fig. 6c). It appeared days before thermal stratification developed. One could see that SST (sea surface temperature) and temperature at 67 m depth coincided until the end of April. The occurrence of earlier shear maxima could be explained by the formation of the stratification in the upper layer caused by the transport of fresher surface water to the area due to northerly wind forcing. Shear maxima became stronger in the second half of May when thermal stratification developed. Strong downwelling and vertical mixing occurred in July as a result of a strong southwesterly wind impulse with the duration of more than a week (Fig. 4). This can be seen as a drop in SST from 21 to 15 °C and occasional high temperature recordings in the deep layer (Fig. 6a). The latter indicates that the upper layer water arrived at the 67 m deep measurement spot. This event is well reflected in the time series of current shear. Deepening of the shear maxima down to 50–55 m depth (Fig. 6c) occurred together with thermocline deepening, as the near-bottom temperature recordings suggest. A precondition for such a rapid drop in SST was the formation of a thin and exceptionally warm surface layer due to atmospheric heat flux (Fig. 6a) and weak wind (Fig. 4) at the end of June. Relaxation of the downwelling occurred in mid-July, and another downwelling developed at the end of July. The linkage between the thermocline and shear maxima was well seen in August when glider observations were available (Fig. 6c). The thermocline and shear maxima reached down to 40 m depth in the beginning and the end of the month, while they were located at 20 m depth in the middle of the month (Fig. 6a and c). The vertical movements of the halocline (Fig. 6d) and thermocline (Fig. 6a and Fig. 6c) and linked shear maxima were synchronized. As thermocline, the halocline had its position also shallower in mid-August and deeper before and after. Note that downwelling was initiated by strong southerly, southwesterly or westerly winds and all events were seen as a SST decrease, likely due to vertical mixing, decrease in salinity at 67 m depth and deepening of the thermocline and halocline and related shear maxima. Relaxation of downwelling occurred when northerly winds or calmer periods prevailed and appeared as an increase in SST and upward movement of both pycnoclines.

Thus, we can conclude that the vertical structure of currents was strongly linked to the varying depths of pycnoclines, which were sensitive to wind forcing.

Table 1. Statistics of the 1-h average ADCP current data from 28 February to 2 September 2020.

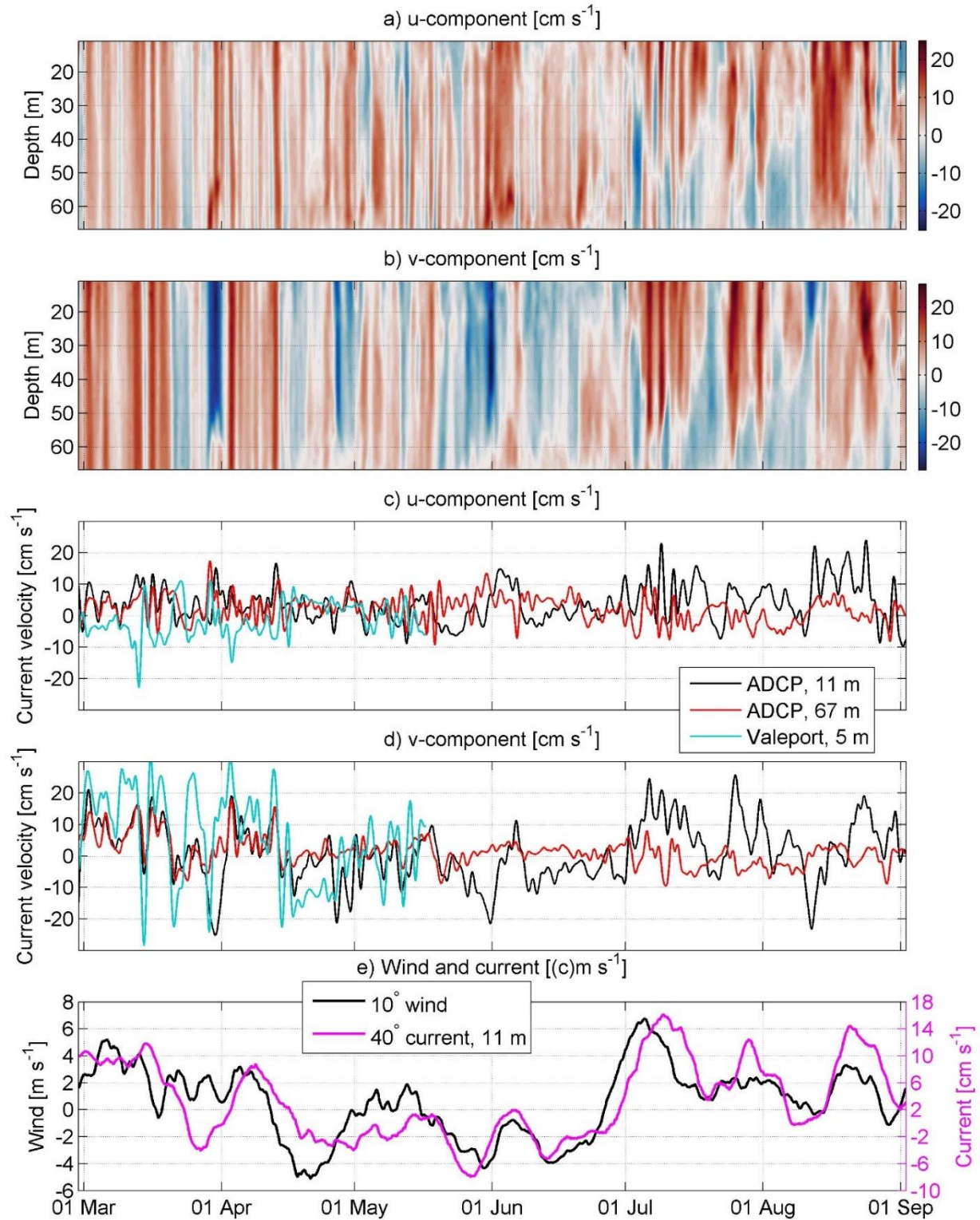| Depth (m)	Mean speed (cm s^{-1})	Mean u (cm s^{-1})	Mean v (cm s^{-1})	Maximum speed (cm s^{-1})	Persistency (%)
10.8	11.3	3.8	1.1	48	35.1
20.8	10.2	4	1.7	44	42.3
30.8	9.5	3.7	1.4	38	41.7
40.8	9	3.4	1.1	37	40.1
50.8	8.8	2.9	0.8	35	34.5
60.8	8.3	2.7	0.7	36	34
66.8	7	1.9	1.2	34	32.7

364

365

366

367

368

Figure 3. Temporal course of the low-pass filtered (36 h) current velocity *u*-component (positive eastward, a and c) and v-component (positive northward, b and d) in the water column (a, b); and in the upper (11 m depth) and deep layer (67 m depth, c, d) in the ADCP and Valeport locations in 2020 (Fig. 1). Low-pass filtered (10 days) wind 10°-component and current 40°-component at 11 m depth in the ADCP location (e).
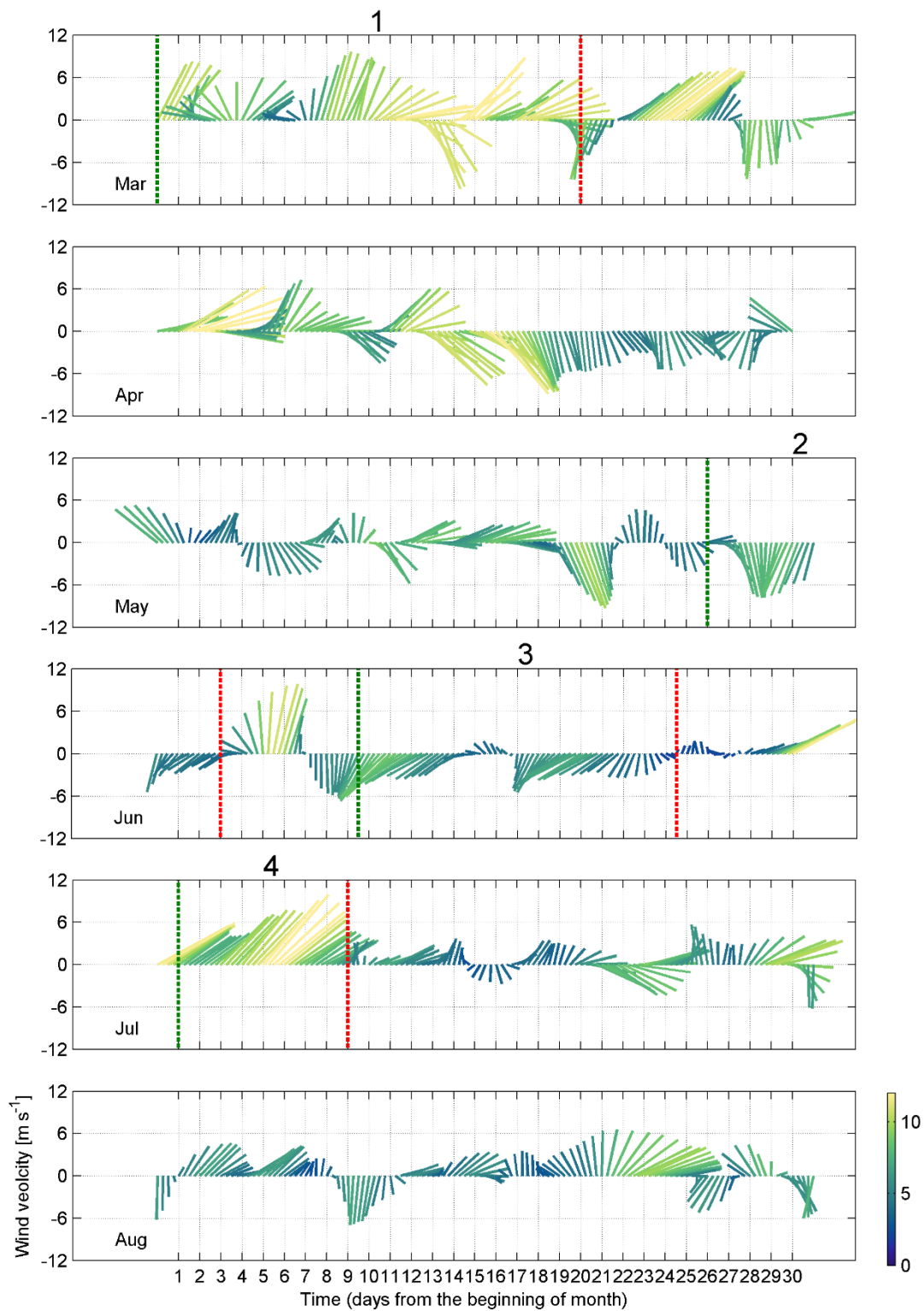
Figure 4. Time series of the 10-m level ERA5 wind data from 1 March to 31 August 2020. Four selected periods are shown: 1) prevailing southwesterly wind, 1–21 March; 2 and 3) prevailing northerly wind, 27 May–4 June and 10–25 June; 4) prevailing southwesterly wind, 2 July–10 July. The green dotted line marks the beginning and red dashed line marks the end of the period. Wind data were smoothed with a 36-h filter. Color scale shows wind speed in m s^{-1}.

14

380
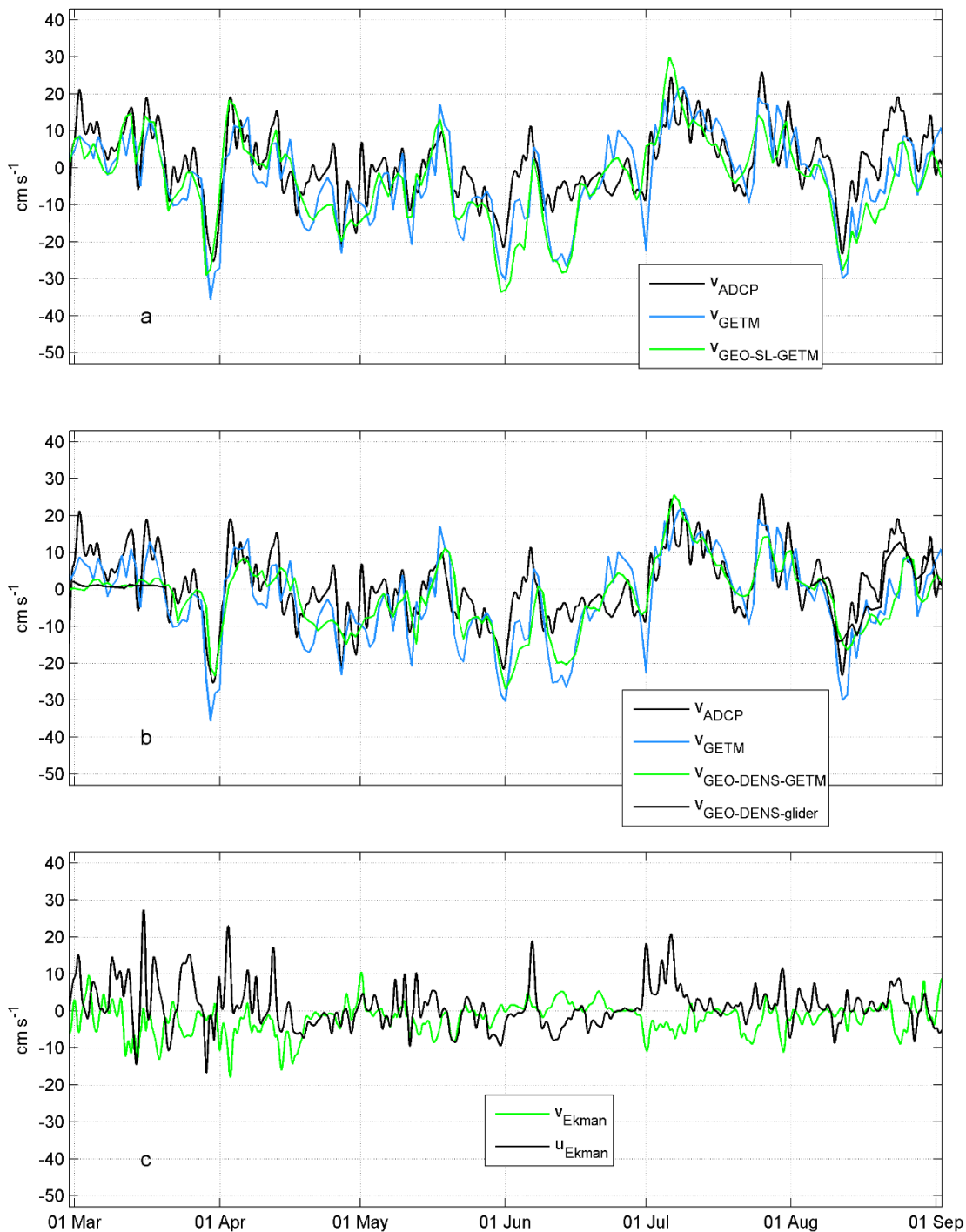
381
Figure 5. Temporal courses of (a, and b panel) current velocity *v*-component (positive northward) measured by
ADCP (V$_{ADCP}$), simulated *v*-component (V$_{GETM}$), estimated from the GETM sea level data (V$_{GEO-SL-GETM}$),
estimated from temperature and salinity data collected by glider (V$_{GEO-DENS-glider}$), estimated from temperature
and salinity data simulated by GETM at 11 m depth (V$_{GEO-DENS-GETM}$). Mean Ekman current *u*-component
(positive eastward) and *v*-component (U$_{Ekman}$ and V$_{Ekman}$) in the depth range 0–11 m (c). Time-series are shown
from March to September 2020 at the ADCP location (see Fig. 1b and c).

388

389
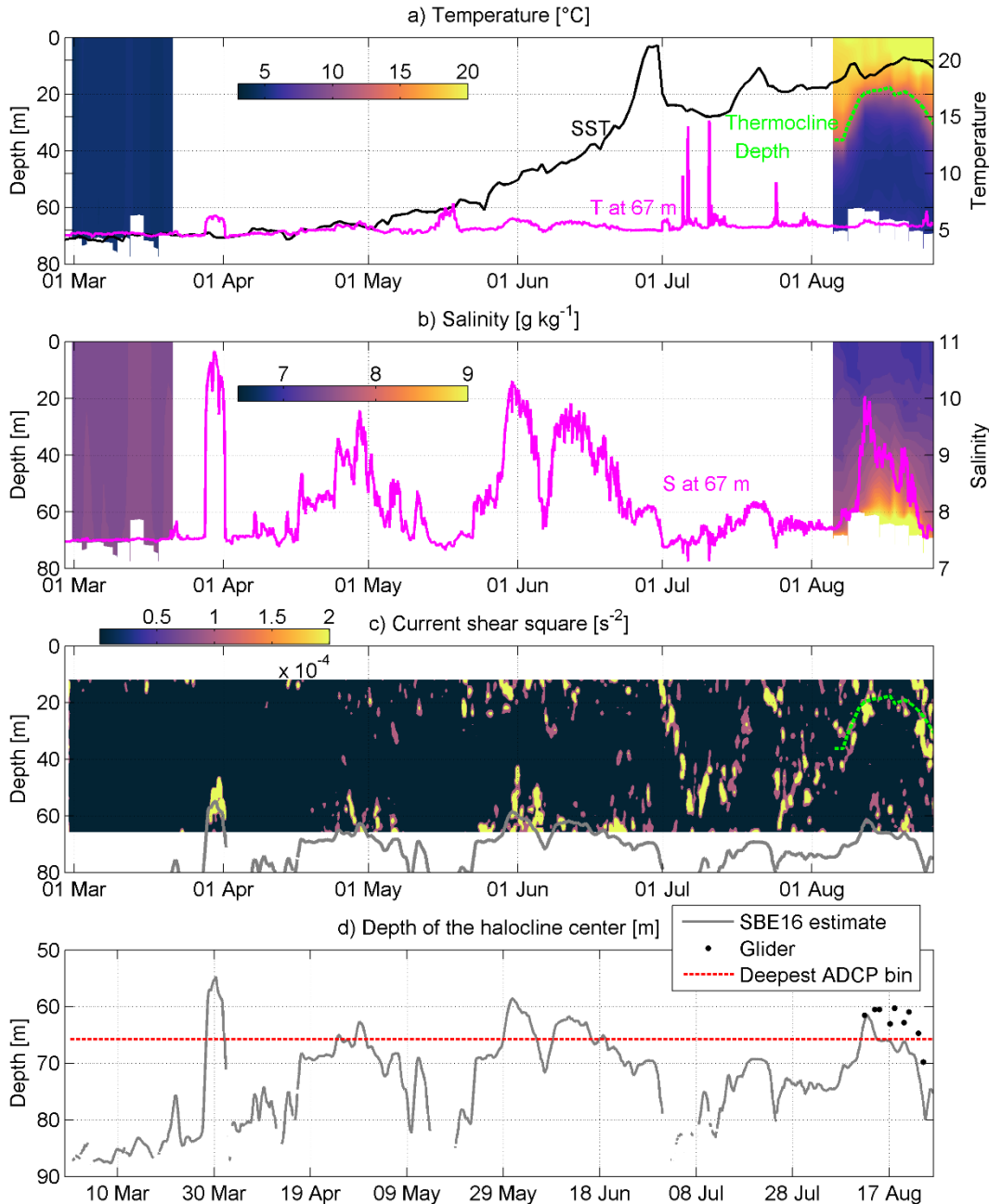
Figure 6. Temporal courses of temperature, salinity, current shear squared and halocline depth in the ADCP location from March to September 2020 (see Fig. 1b and c). (a) Temporal course of sea surface temperature (SST) and temperature at 67 m depth; temporal course of the vertical distribution of mean temperature in March and August calculated from glider data (color scale). Depth of the thermocline center is shown as red dashed line. (b) Temporal course of salinity at 67 m depth; temporal course of the vertical distribution of mean salinity in March and August calculated from glider data (color scale). Mean temperature and salinity profiles were calculated for each glider passing within the 3.7 km zonal window around the ADCP location. Depth of the thermocline center is shown as red dashed line. (c) Temporal course of the vertical distribution of current shear

16

398 squared and depth of the halocline center (grey line). (d) Depth of halocline center, calculated from SBE16 data
399 and in August from glider data. Depth of deepest ADCP bin is also shown (red dotted line).

3.2 Quasi-permanent circulation patterns

401 In the previous chapter, we demonstrated the importance of wind forcing and stratification for the
402 currents. Next, we describe the current structure during the quasi-steady forcing periods. We have
403 selected four periods of 8–21 days duration with relatively stable forcing (see Fig. 4) to analyze the
404 mean measured and simulated flow structure in the ADCP and Valeport locations (Fig. 7) and along
405 the zonal section (Fig. 8). Likewise, we investigated the horizontal structure of ~~lateral~~ simulated flow
406 ~~structures~~ in the three forcing cases in three layers: upper layer (5 m), intermediate layer (40 m) and
407 deep layer (110 m) (Figs. 9–11).

408 The persistency of the measured currents in the ADCP location was very high in all selected periods
409 (Table 2). Only during the fourth period, the persistency was lower than 50% below the seasonal
410 thermocline. Particularly high persistency (82–94%) occurred in the first and second periods. Thus,
411 measured currents during the quasi-steady forcing have much higher persistency than overall of the
412 time series (see Table 1).

413 Barotropic flow to the northeast prevailed throughout the water column at the ADCP location in the
414 first period (1–21 March) when south-westerly wind prevailed (Fig. 7a,~~and~~ b and c). Even stronger
415 mean current to the north-northwest was registered at 5 m depth at the Valeport location (Fig. 7b~~3c and~~
416 ~~d~~). Latter indicates the boundary effect near the Saaremaa Island~~.~~, ~~T~~the current was directed along the
417 coast (Fig. 1c). Mean flow was to the south in the upper layer (Fig. 7g) during the second period (27
418 May–4 June) when northerly wind prevailed (Fig. 7e), to the southeast below the thermocline and to
419 the east below the halocline (Fig. 7e ~~and~~ f and g). In general, a similar current pattern occurred in the
420 third period (10–25 June) when north-westerly wind prevailed (Fig. 7i, ~~and~~ j and k). Due to relatively
421 strong south-westerly wind forcing in the fourth period (2–10 July), flow to the northeast prevailed in
422 the upper layer and to westerly directions below the thermocline (Fig. 7m and n).

423 In conclusion, a pattern typical for the downwelling event – current to the northeast along the boundary
424 and towards the shore in the upper layer (Fig. 7n and o) and seaward current to the southeast in the
425 deep layer (Fig. 7n) occurred during southwesterly wind domination (Fig. 7f~~m and j~~). On the contrary,
426 a pattern typical for the upwelling: ~~The~~ the flow was to the south along the coast in the upper layer
427 (Fig. 7g and k) ~~along the coast~~ and onshore (east) in the deeper layers (Fig. 7f, j, g and k)~~, which is~~
428 ~~typical for the upwelling cell in the case of northerly winds (Fig. 7e and in)~~ were observed in the case
429 of northerly winds (Fig. 7e). These vertical patterns (downwelling and upwelling) of the current
430 velocity were also well captured by the numerical model (Fig. 7g, k and o)~~, although the magnitude of~~
431 ~~the mean simulated velocity occasionally deviated from the measured values. Likewise, t.~~ The stronger
432 mean measured current at 5 m depth near the boundary ~~at the~~ (Valeport location), was well reproduced
433 by the model (Fig. 7b and c). The mean adjusted ~~G~~geostrophic velocit~~iesy~~ profiles based on simulation
434 data had a quite similar vertical structure compared to the measured mean velocit~~yies~~ profiles in all
435 periods (Fig. 7, ~~third~~ second and fourth columns). Thus, currents were generally in geostrophic balance
436 during the quasi-steady periods. The transition from one state to another has likely an ageostrophic
437 nature, as wind is the main driver for the change.

438 Next, to understand the larger scale circulation dynamics during the periods, we analyze the vertical
439 ~~(Fig. 8) and horizontal (Fig. 9–11)~~ structure of the mean meridional component of currents (Fig. 8) in
440 the section along the latitude of the ADCP location (Fig. 1b) and the horizontal structure of mean
441 currents at selected depths (Figs. 9–11) in the Eastern Gotland Basin (Fig. 1b) using simulated current

442 data. The current data are averaged within the same time windows with relatively stable wind forcing
443 as analyzed above.

444 The structure of the meridional component of currents in the section is characterized by high spatial
445 and temporal variability (Fig. 8). The unidirectional flow prevailed in most of the section down to the
446 halocline or even deeper in the case of no thermal stratification and southwesterly winds (first period)
447 (Fig. 8a). The northward current along the eastern boundary with a cross-coast extent of 10 km was
448 especially strong. This strong boundary current was also registered by the Valeport (Fig. 3d). The
449 strong maxima of the northward flow can be found between 20.5°–21.0° E, 18.6°–19.3° E and around
450 17.6° E. The strong southward flow prevailed between 21.0°–21.3° E, 19.4°–20.0° E, and 17.6°–18.6°
451 E. Horizontal flow structure in the Eastern Gotland Basin consisted of the two stronger current zones
452 above the halocline (at a depths of 5 and 40 m), northward current along the eastern bottom slopeundary
453 and southward current alongin the bottom slope in the western middle part of study area (Fig. 9a and
454 b). The two zones were connected with several cyclonic cells. The northward flow below the halocline
455 at a depth of 110 m (Fig. 9c) coincided with the flow in the upper layer along the bottom slope in the
456 Eastern Gotland Basin area but was forced to the westward trajectory by bathymetry in the northern
457 area.

458 The mean meridional currentflow patterns were very similar in the following two periods (second and
459 third) of prevailing northerly winds and the presence of thermocline. In both cases, the zonal scale of
460 the southward flow around the ADCP location was 10–15 km (Fig. 8b and c). The flow did not extend
461 to the eastern boundary, a narrow northward flow with a width of 5–10 km occurred along the coastal
462 slope. The width of the southward flow near the western boundary of the section was about 30 km. In
463 between, several circulation cells with zonal scales of 20–60 km can be distinguished in the cross-
464 section (Fig. 10a). The horizontal structure of the flow below the thermocline at a 40 m depth in the
465 Eastern Gotland Basin revealed a strong southward current in the eastern part of the area in the second
466 period (Fig. 10b). The current swirled, split into two branches and re-merged back to one in several
467 locations. The southward flow below the thermocline (40 m depth) coincided with the offshore branch
468 in the upper layer in the central area of the basin (Fig. 10a and b). Sub-halocline flow revealed strongest
469 northward current along the bottom slope and strongest cyclonic cell in the Eastern Gotland basin
470 among the selected periods (Fig. 10c).

471 The flow pattern in the case of strong southwesterlies dominance (fourth period) under stratified
472 conditions revealed a strong northward current component along both boundaries of the section (Fig.
473 8d). In between, the strong southward flow occurred in the surface layer. Similarly, to the northerly
474 wind prevailing, complicated three-layer structure with variable horizontal patterns in the zonal scale
475 of 20–60 km occurred. Flow to the southeast prevailed for most of the study area in the upper layer (5
476 m depth), except in the eastern boundary zone, where a strong northeastward downwelling related flow
477 occurred (Fig. 11a), as also was observed in our ADCP mooring data (Fig. 7n). A strong current
478 occurred also in the Irbe Strait towards the Gulf of Riga. Downwelling related flow along the eastern
479 coast was also observed at 40 m depth (Fig. 11b). In the deep layer below the halocline (110 m depth),
480 northward current along the eastern bottom slope and cyclonic cells in the Eastern Gotland Basin were
481 observed (Fig. 11c).

482

483 Due to seasonality in forcing, variations in the circulation in this time scale can be expected. Next, we
484 analyze the vertical distribution of monthly mean (April, July and December) and annual mean
485 meridional velocity component (Fig. 12) along the zonal section (Fig. 11) at ADCP latitude based on

486 simulation data from September 2010 to August 2020. The boundary current alongin the eastern coastal
487 slope occurreds year-round (Fig. 12d) but wasis the strongest in winter (Fig. 12c). This is related to the
488 wind regime: southwesterly winds prevail more in winter but are less frequent in spring and summer.
489 The seasonal signal can be found in the whole section (Fig. 12a, b and c). Well defined large cyclonic
490 gyres in the Northern Baltic ProperEastern Gotland Basin can be found in winter (Fig. 12c), while in
491 spring and summer (Fig. 12a and b), the mean current structure is characterized by the smaller scale
492 zonal features and weaker flow. However, it is noteworthy that the mean flow is to the north along the
493 eastern coastal slope in all seasons.

494

495 **3.3 Sub-halocline current**

496 As shown above, Ccyclonic gyre was present below the halocline in the Eastern Gotland Basin in all
497 selected periods (Figs. 9–11). The flow in this cyclonic system was especially strong along the eastern
498 slope of the Eastern Gotland Basin. The northern branch of this circulation system is connected to the
499 clearly distinguishable northward current. The position and magnitude of the current varied under
500 different conditions. The current was stronger and meandered to west at the shallower area between
501 Gotland and Fårö Deep in the case of northerly wind while it was slower, and the meandering did not
502 occur in the case of southwesterly winds. To confirm the simulated cyclonic circulation in the Eastern
503 Gotland Basin and the northward flowing current towards the Northern Deep, the Argo float trajectory
504 and the mean current field between 105–135 m depth were plotted in the same time frame from 15
505 August 2013 to 15 August 2014 (Fig. 13a). The general features in the simulated mean currents and
506 the Argo float trajectory agreed well. The Argo float first completed two circles (smaller and larger) in
507 the Eastern Gotland Basin and then headed to the north. The float arrived and was recovered in the
508 shallower area between the Fårö and Nothern Deep. This sill is an important location for the deep layer
509 water renewal in the Northern Baltic Proper (see bathymetry in Fig. 14), as this is the only remarkable
510 passage to the north below 100 m depth (see bathymetry in Fig. 14). The sill is located slightly south
511 of the selected section along the latitude of the ADCP deployment.

512 The mean simulated meridional flow to the north over the still was concentrated in a narrow cell with
513 a zonal scale of 5–6 km in 2010–2020 (Fig. 15a). The flow was especially strong when northerly winds
514 prevailed, e.g., in the second period from 27 May to 4 June 2020 (Fig. 15b). The 2010–2020 mean
515 density field sloped downward in the left (west) of the flow (Fig. 15a and b), typical for a gravity
516 current (Fig. 15a b). The meridional current velocity (C_T) in the trench was mostly positive
517 (northward) and in the range of 10–20 cm s^{-1} during the study period March–September in 2020 (Fig.
518 15c). The C_T was reversed in the first half of July, which coincided with the strong southwesterly wind
519 impulse (Fig. 4). The time series of C_T for 2010–2020 (Fig. 15d) revealed many reversal events, but
520 the long-term mean meridional velocity was 10 cm s^{-1} to the north. Reversals were most frequent in
521 November–December when the monthly mean southward C_T was 6–7 cm s^{-1} and rarer in March–May
522 when monthly averages were in the range of 12–14 cm s^{-1}. Thus, the deep layer water renewal in the
523 Northern Baltic Proper is most active in the spring period and more restricted in late autumn–early
524 winter. The best correlation (r^2=0.25, p<10^{-100}, n=3838) between 10-day low-passed current velocity
525 at the sill and wind was found with the wind from ENE (70°) with a delay of 6 days. This is another
526 confirmation that prevailing southwesterly winds slow down or reverse the C_T and prevent deep water
527 renewal in the Northern Baltic Proper.
528

529 **Table 2.** Persistency (%) of the <u>measured</u> currents <u>in the ADCP location</u> at the selected depths during the
530 selected periods: 1 March to 21 March (1); 27 May to 4 June (2); 10 June to 25 June (3); 2 July to 10 July (4)
531 in 2020.

Period/ depth (m)	1	2	3	4
10.8	84.8	82	75.8	83.1
20.8	88.8	92.3	76.9	78.9
30.8	88.8	94	66.2	54.8
40.8	88.6	92.5	62.1	41.3
50.8	89.3	89.9	61.4	24
60.8	87.7	91.1	70.1	27.5
66.8	87.2	86.1	64.1	4.7

532
533
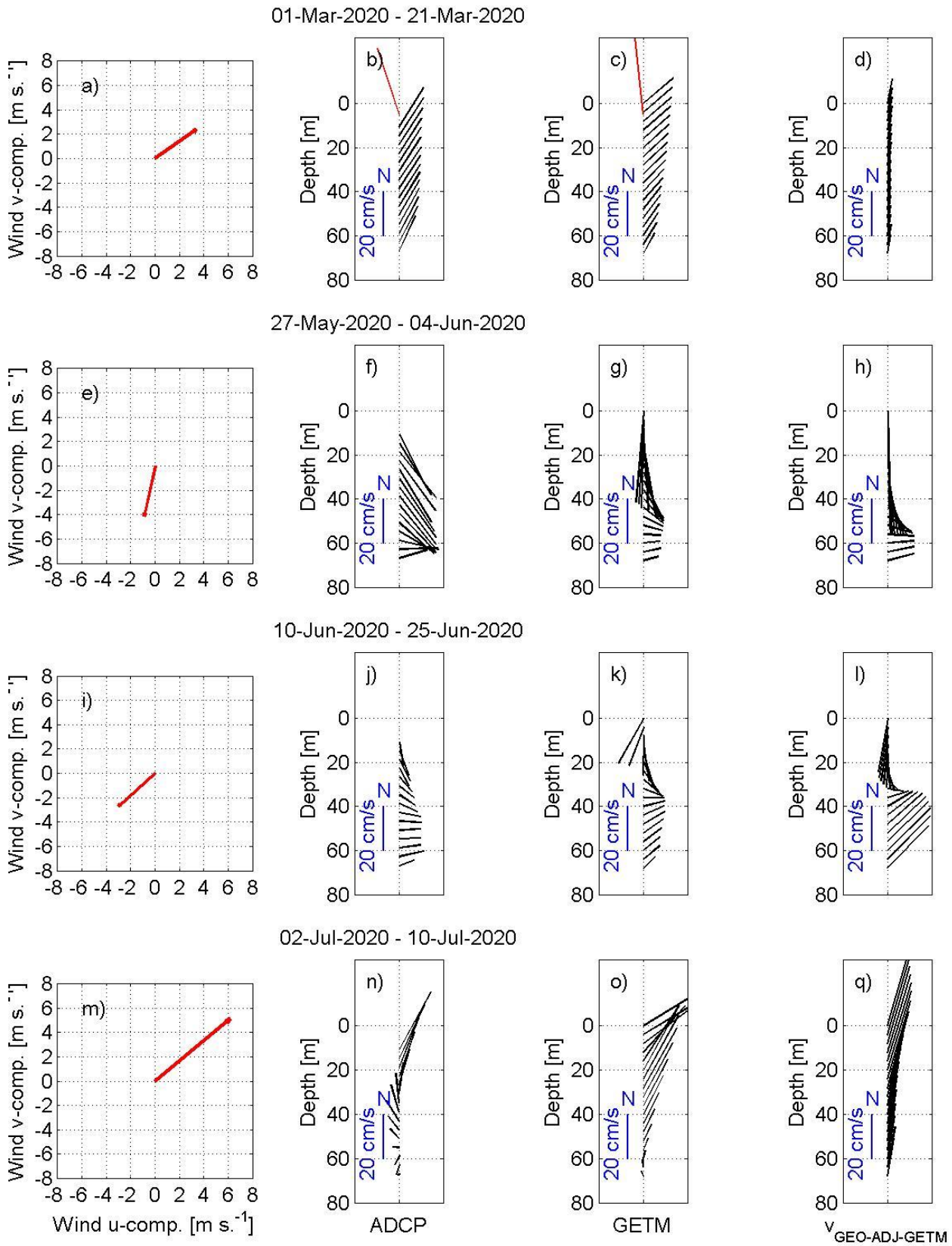
Figure 7. The mean resultant wind vectors (a, e, i, m), mean profiles of current velocity vectors calculated from ADCP data (black arrows, b, f, j, n) and~~, mean current velocity vector based on Valeport data at 5 m depth (b,~~

21

537 ~~red arrow),~~ mean simulated current velocity vectors at the ADCP location (c, g, k, o) ~~and at the Valeport location~~
538 ~~(c, red arrow)~~ are shown for selected periods (Fig. 4). <u>The mean current velocity vector at 5 m depth based on</u>
539 <u>Valeport data (b, red arrow) and mean simulated current velocity vector at the Valeport location (c, red arrow)</u>
540 <u>for the first time period are shown.</u> On the right panels, mean adjusted geostrophic velocity vectors $V_{GEO\text{-}ADJ\text{-}}$
541 $_{GETM}$ (d, h, i, q) are shown.
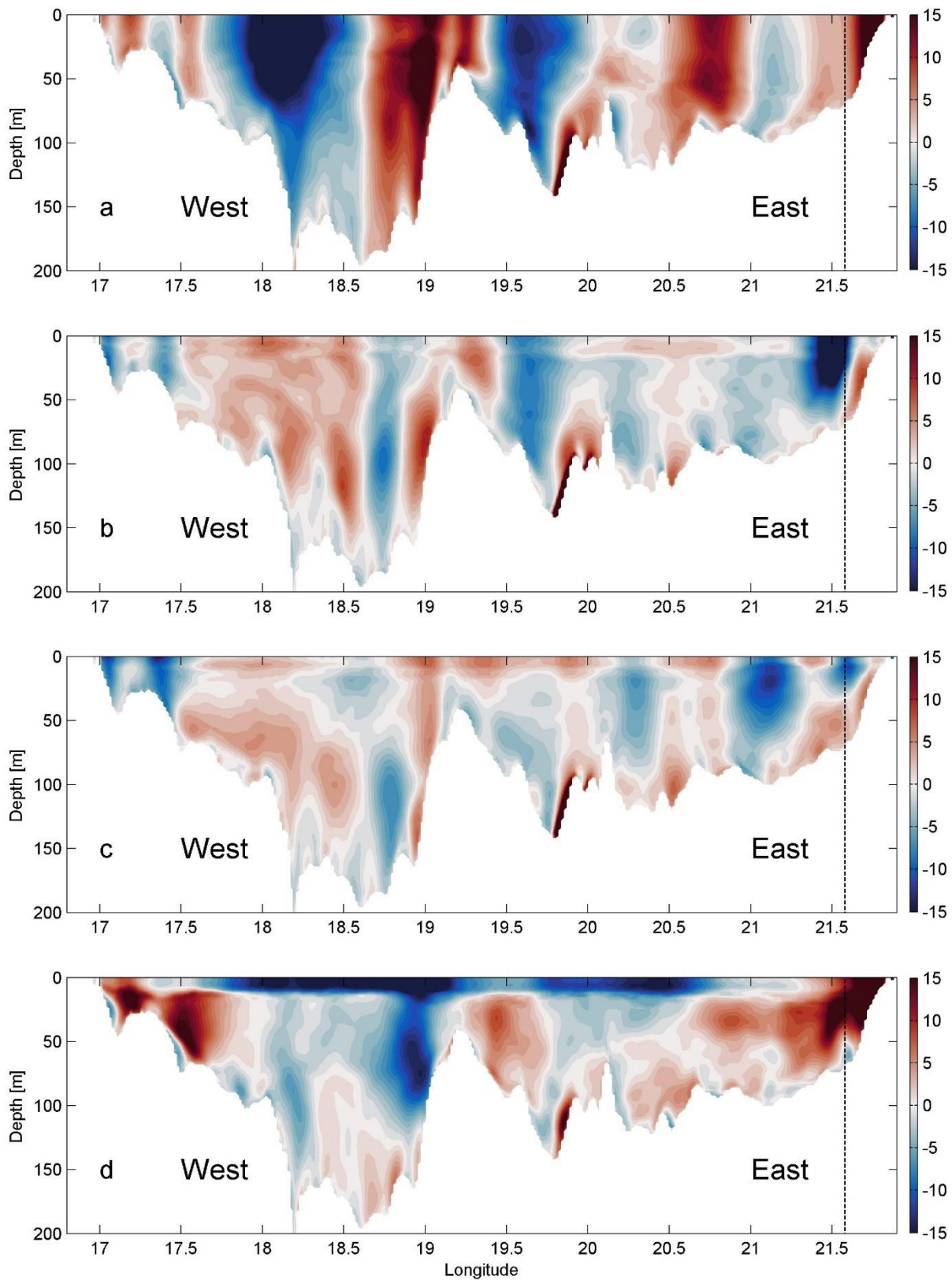
542
Figure 8. Vertical distribution of <u>simulated</u> mean meridional current velocities for four selected periods<u>: a) 1–</u>
544 <u>21 March, b) 27 May–4 June, c) 10–25 June and d) 2 July–10 July</u> <u>2020</u> (see Fig. 4) along the ADCP deployment
545 latitude (Fig. 1b). Color scale displays meridional velocity (positive northward) in cm s^{-1}. Vertical dotted lines
546 show the ADCP location.

547
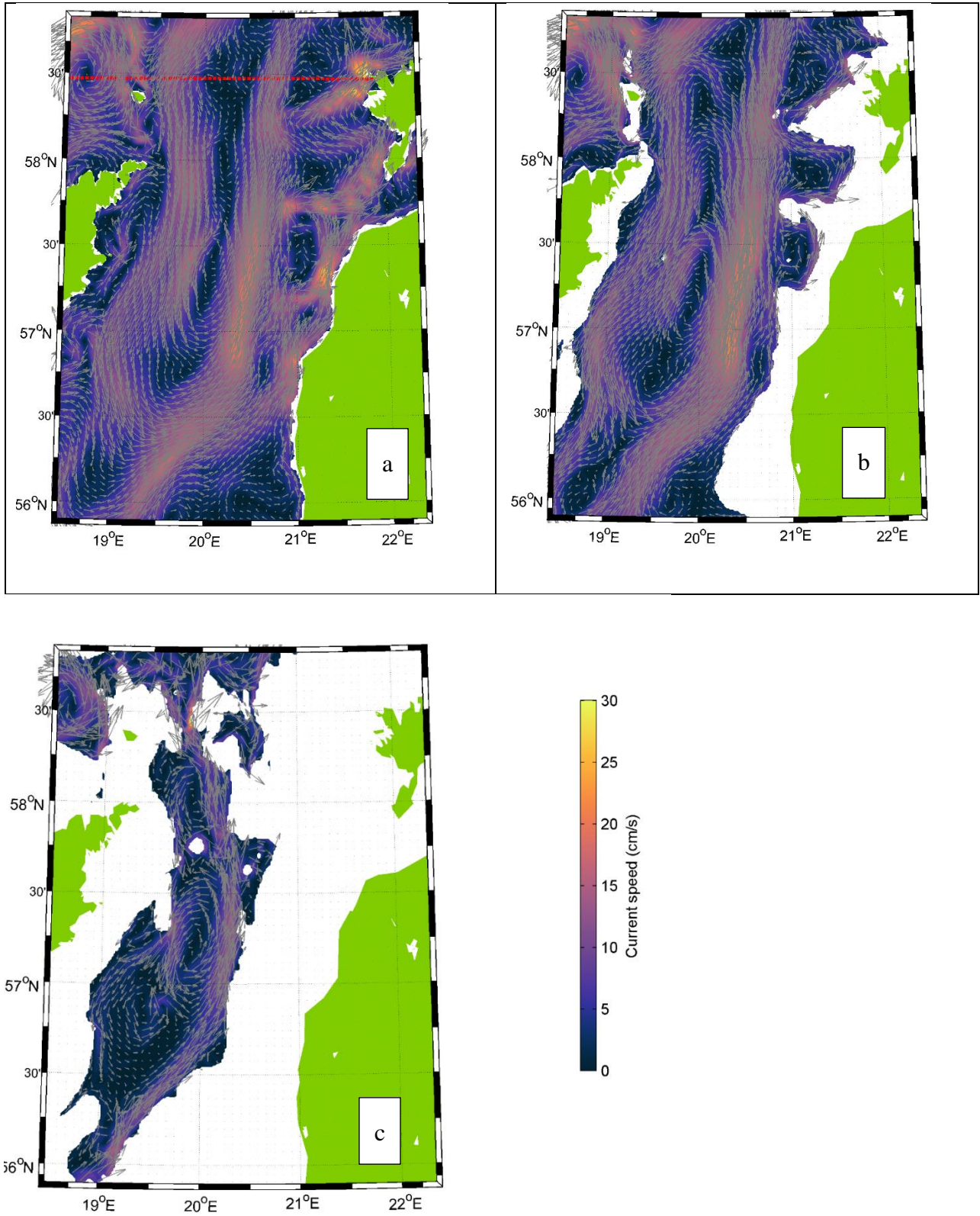
548
549 **Figure 9.** Mean <u>simulated</u> currents in the case of prevailing south-westerly winds from 1 March to 21 March
550 2020, without thermocline at 5 m depth (a), 40 m depth (b) and 110 m depth (c). Color scale shows current speed
551 in cm s⁻¹. <u>Red dashed line on panel (a) shows the location of the transect presented in Figs. 8 and 12.</u>

552

553
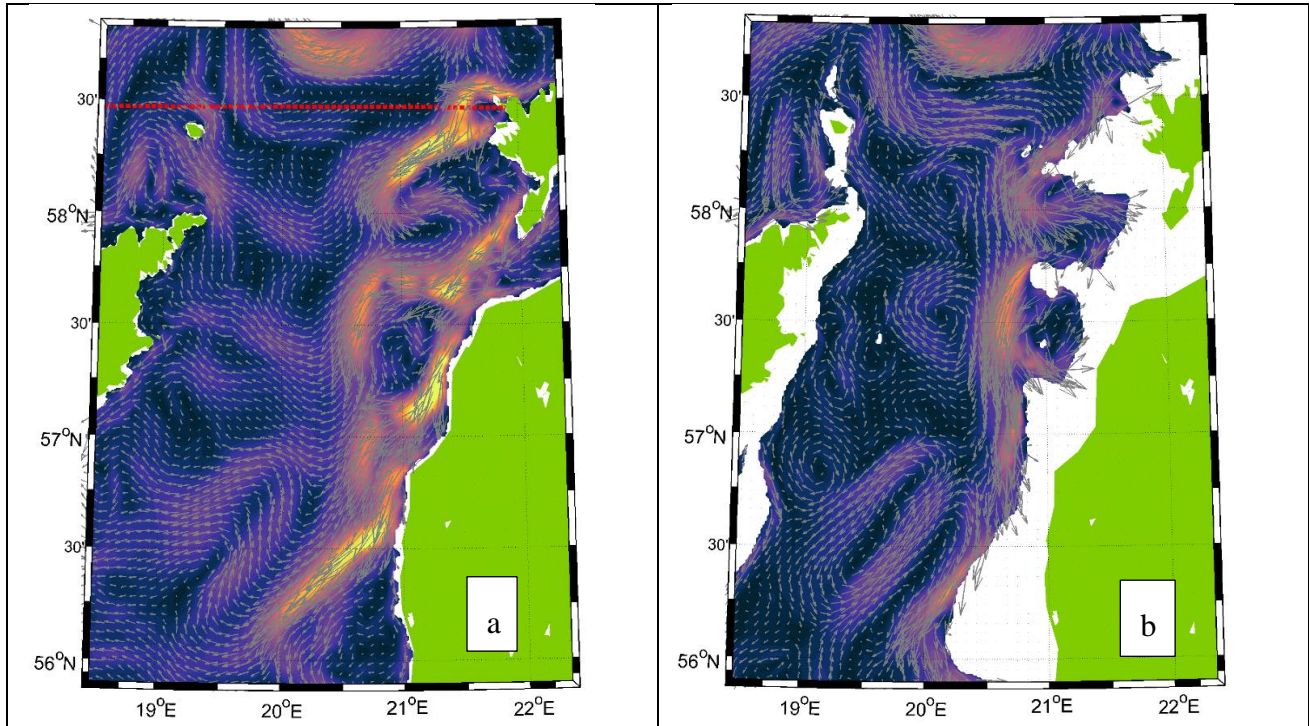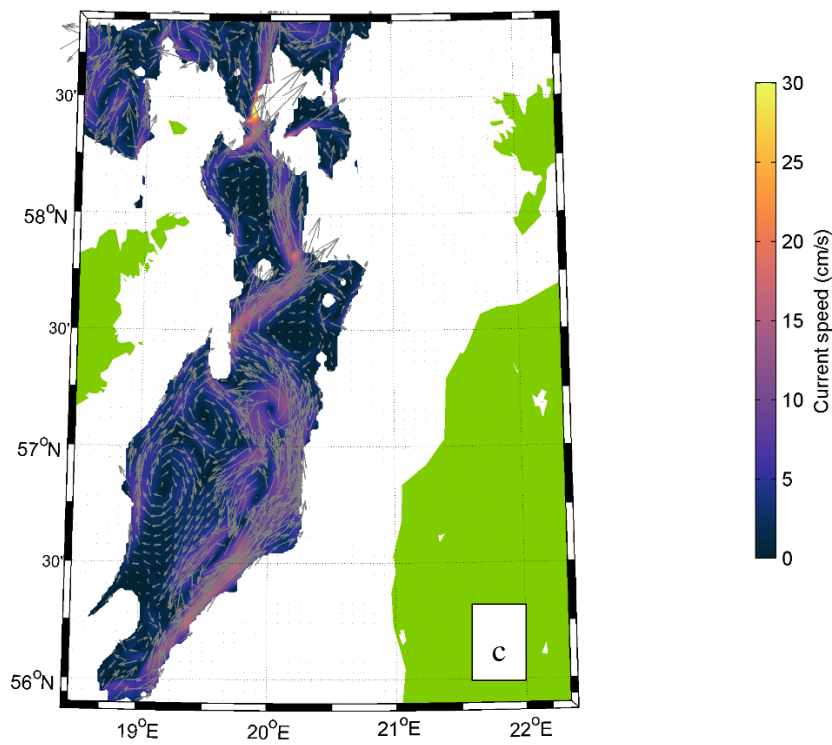
554
555
556
557 **Figure 10.** Mean <u>simulated</u> currents in the case of prevailing northerly winds from 27 May to 4 June 2020, with
558 thermocline at 5 m depth (a), 40 m depth (b) and 110 m depth (c). Color scale shows current speed in cm s^{-1}.
559 Red dashed line on panel (a) shows the location of the transect presented in Figs. 8 and 12.
560

561
562
563
564
565
566
567
568
569
570
571
572
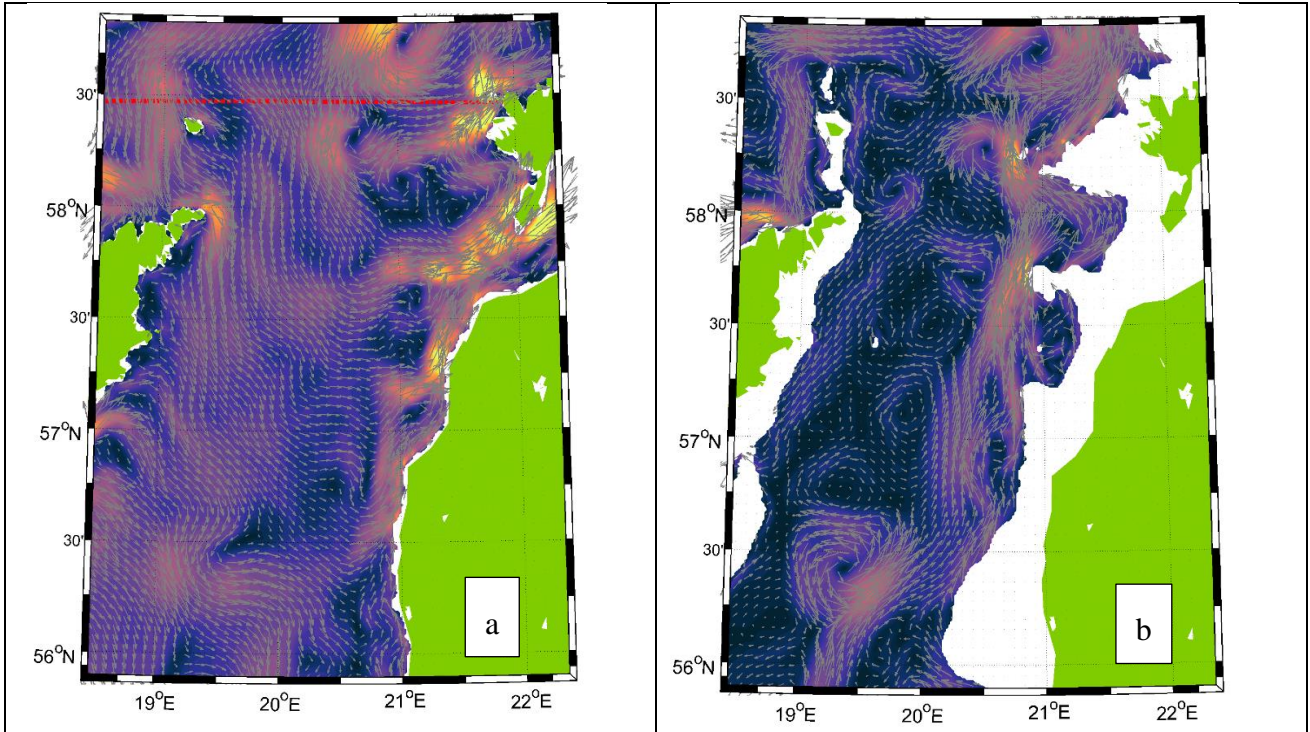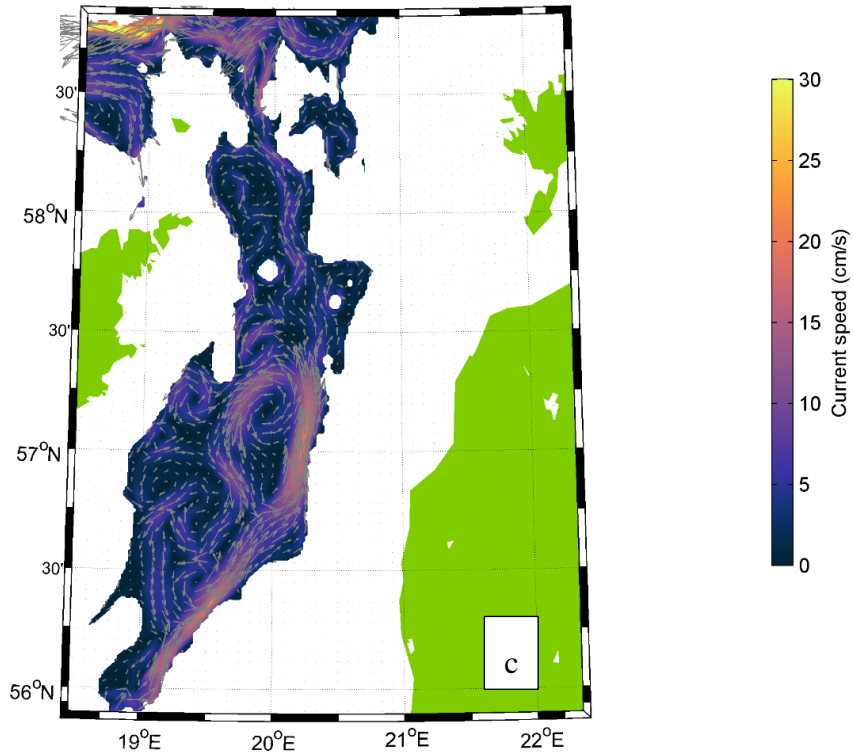
573
574 **Figure 11.** Mean <u>simulated</u> currents in the case of prevailing south-westerly winds from 2 July to 7 July 2020,
575 with thermocline at 5 m depth (a), 40 m depth (b) and 110 m depth (c). Color scale shows current speed in cm
576 s^{-1}. <u>Red dashed line on panel (a) shows the location of the transect presented in Figs. 8 and 12.</u>
577
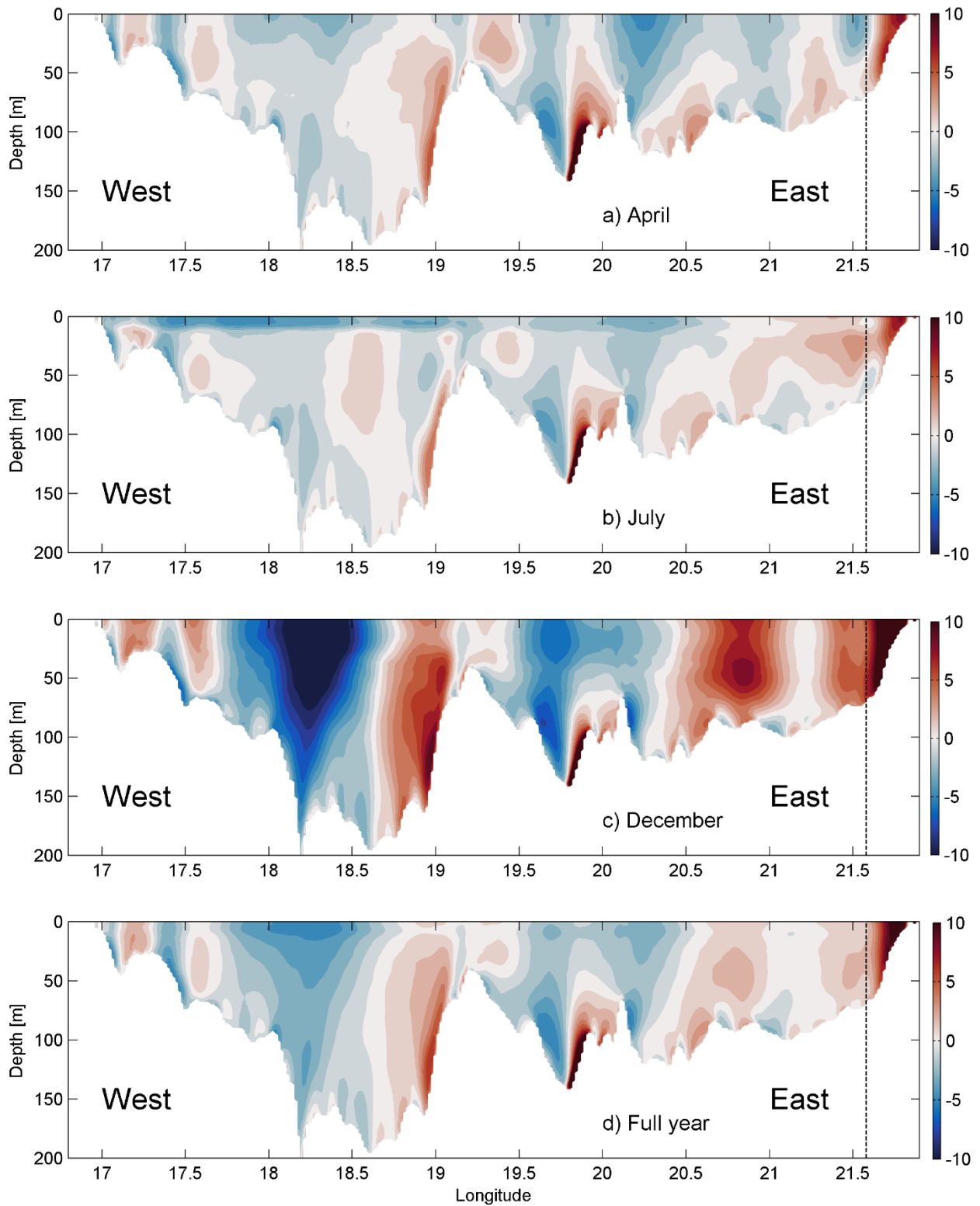
Figure 12. Vertical distribution of monthly mean (April, July and December) and annual mean meridional velocities (positive northward) along the zonal section at ADCP latitude based on simulation data from

581   September 2010 to August 2020. Color scale shows meridional velocity in cm s⁻¹. Vertical dotted lines show
582   the ADCP location.
583
584
585
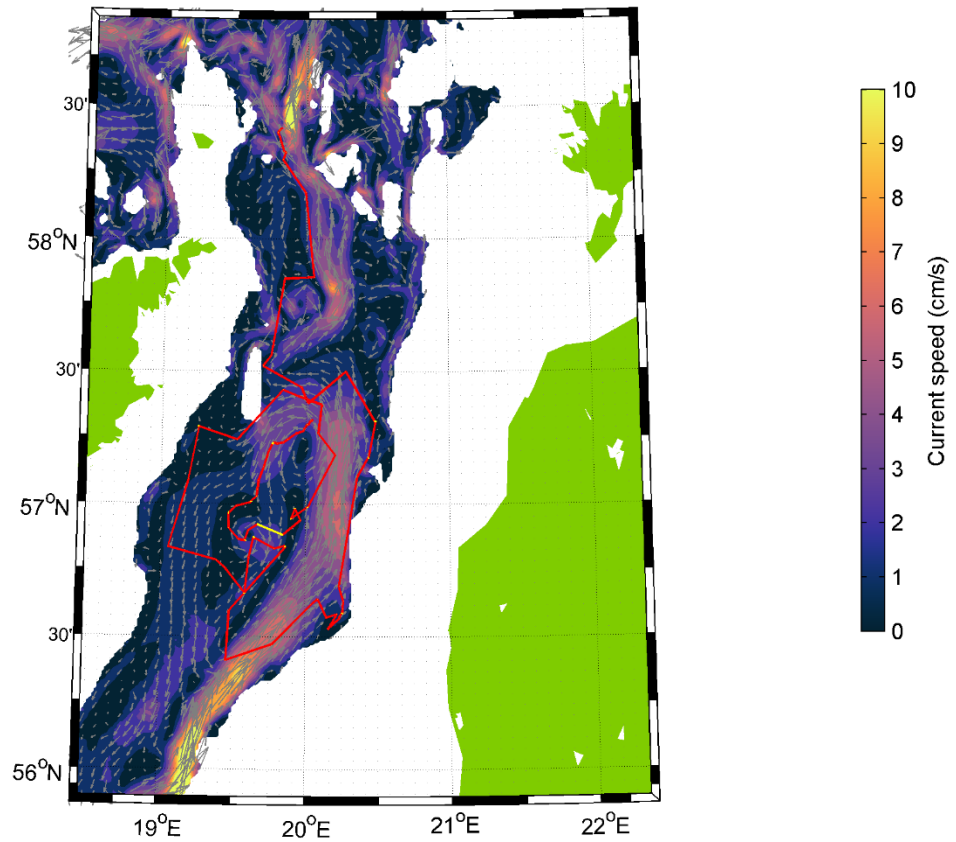
586
587   **Figure 13.** Mean current field between 105–135 m depth based on simulation data and ARGO (WMO number
588   6902014) float trajectory during the period 15 August 2013–15 August 2014 in the deep layer (within its parking
589   depth range 105–135 m, shown in red). Only one longer period occurred, when the float drifted on the surface
590   (shown in white). Color scale shows current speed in cm s⁻¹.
591
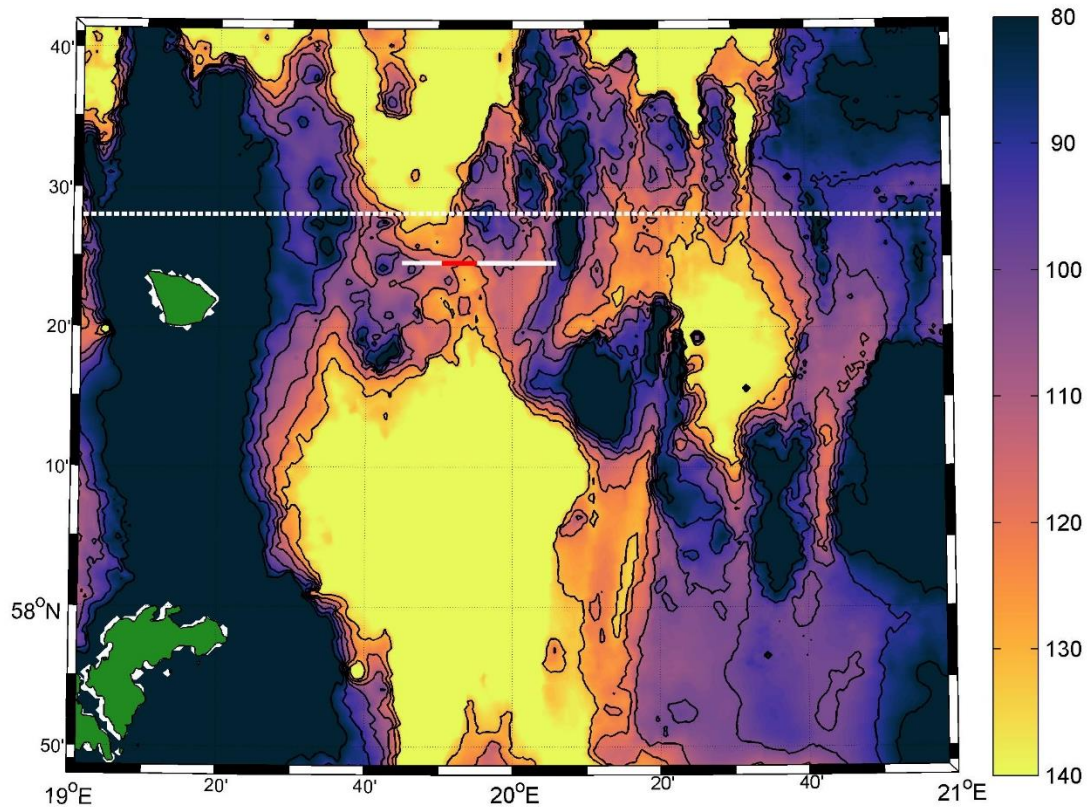
592
Figure 14. Bathymetry between Farö Deep and Northern Deep (see Fig. 1b). Color scale shows the depth in
meters. White dashed line marks the section along the ADCP deployment latitude (Fig. 1b). White line marks
the section in Fig. 15a, and red line indicates time-series calculation range for Fig. 15b–c.
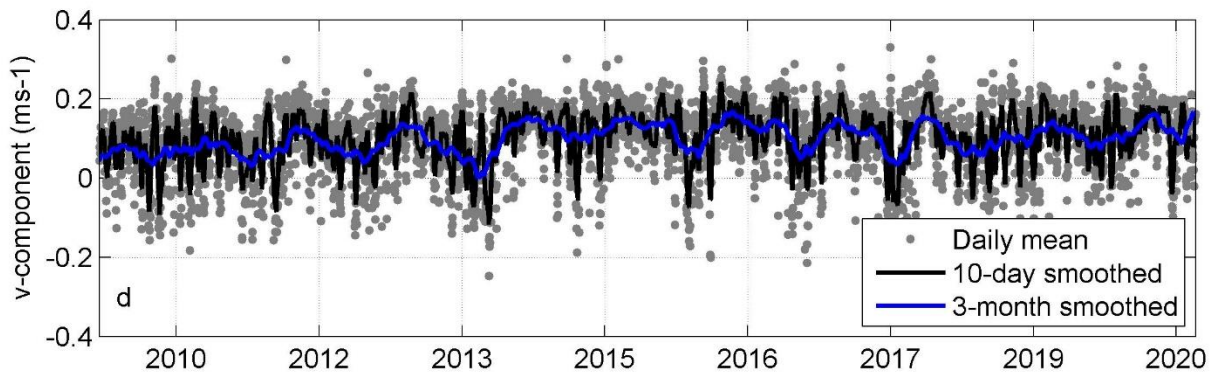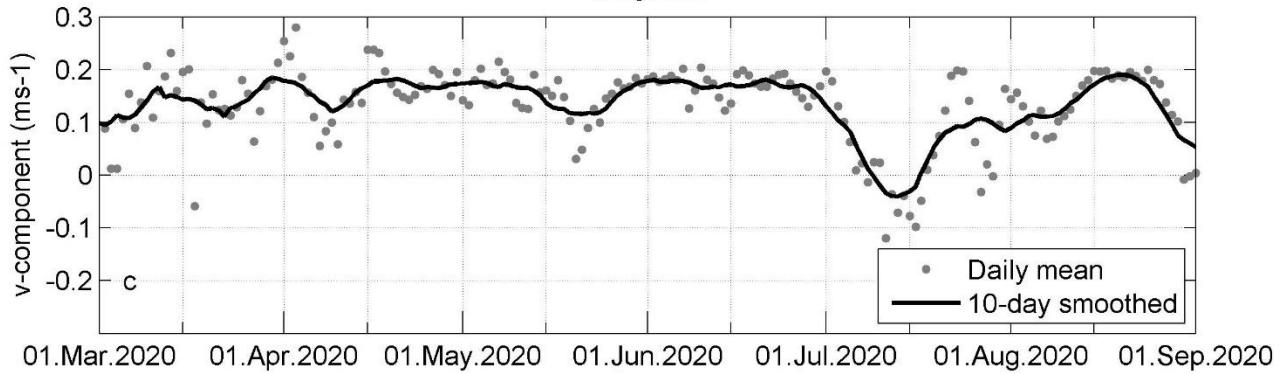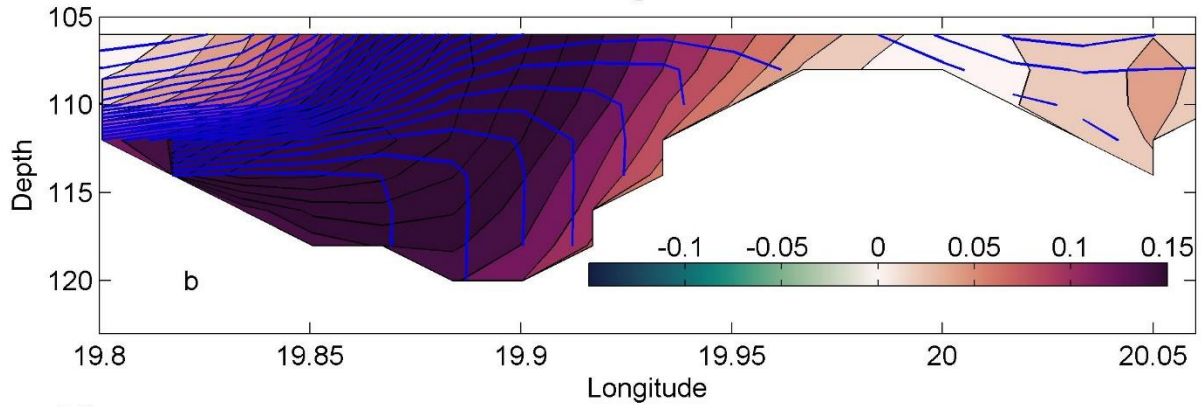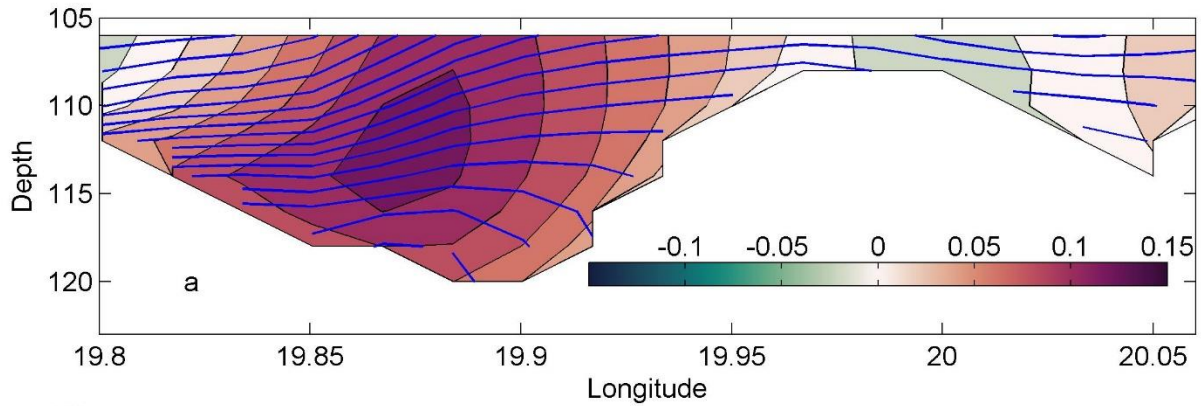
Figure 15. (a) mean simulated meridional current component *v* <ins>(positive northward)</ins> and density isolines at
section below 105 m depth (the section location is shown as red line in Fig. 14) in 2010–2020, (b) mean

599 simulated meridional current component *v* and density isolines at section below 105 m depth from 27 May to 4
600 June 2020 during a northerly wind impulse. In color scale contours with step of 2 cm s^{-1} show current *v*-
601 component (m s^{-1}, positive northward) and blue lines show density isolines with a step of 0.05 kg m^{-3}. (c) time-
602 series of *v* component below 105 m at the sill. Dots marks the daily mean and bold line 10-day smoothed *v*-
603 component from March to September. (d) time-series of *v* component below 105 m at the sill. Dots marks the
604 daily mean, bold black line 10-day smoothed and bold blue line 3-month smoothed *v*-component in the period
605 2010–2020.
606
607

4 Discussion

609 Moorings carrying ADCP and single-point current meter, and underwater glider surveys were applied,
610 together with numerical modeling to investigate circulation in the Baltic Proper.

611 Strong linkage between the vertical location of the current shear maxima and the two pycnoclines was
612 observed. The same finding was reported in the Gulf of Finland (Suhhova et al., 2018). The current
613 shear maxima in the Gulf of Finland were related to the along-gulf estuarine circulation and its
614 alterations. In the present case, the shear maxima were related to the currents along the basin axis and
615 the coastal downwelling and upwelling circulation structures. The separation of the cross-shelf flow
616 by a pycnocline has been documented in several other coastal systems (Davis, 2010; Gilcoto et al.,
617 2017; Villacieros-Robineau et al., 2013).

618 Boundary current in the upper layer along the eastern coast was observed. The current was well
619 correlated with the wind. The wind regime in the area is the combination of the global circulation and
620 specific direction-dependent boundary-layer effects, which results in domination of winds along the
621 axis of the Baltic Proper (Soomere & Keevallik, 2001). Along-axis wind causes the Ekman current
622 (Ekman, 1905) to the right from wind direction in the upper layer, i.e., a flow across the basin axis.
623 The resulting convergence (divergence) in the case of southwesterly (northerly) winds at the eastern
624 coast causes across-axis sea level gradient and the upper pycnocline inclination, which in turn cause
625 horizontal pressure gradient, and results in a geostrophic flow to the north (south) in the upper layer.
626 Boundary currents forced by the pressure gradient caused by wind-driven divergence/convergence are
627 common in coastal systems (Berden et al., 2020; Longdill et al., 2008; H. Wu et al., 2013). The
628 geostrophic current velocity is well agreed with the total current velocity profiles. Thus, the current
629 along the boundary was generally in the geostrophic balance, but across-shore ageostrophic flow
630 created preconditions for this geostrophic coastal current.

631 Circulation rapidly reacted to the wind forcing. Persistency of the current for 6 months was rather low
632 (30–40%) due to variability in the wind forcing. The estimated persistency from long-term numerical
633 simulations data in the same area above the halocline was 70–80% in 1981–2004 (Meier, 2007) but
634 around 30–40% in the upper layer in 1958–2007 (Jędrasik & Kowalewski, 2019). However, the quasi-
635 steady circulation patterns detected under different wind and stratification conditions were high-
636 persistent, mostly >75%.

637 The mean cyclonic circulation in the upper layer of the Baltic Proper has been reported by many
638 modeling studies (Hinrichsen et al., 2018; Jedrasik et al., 2008; Jędrasik & Kowalewski, 2019; Meier,
639 2007; Placke et al., 2018). However, the magnitude of the long-term mean circulation patterns had a
640 considerably lower magnitude than the quasi-steady circulation structures presented in this study.
641 Likewise, the current direction of quasi-steady patterns varied and differed considerably from the long-
642 term mean. The circulation structures in this timescale also differ from the long-term mean because of

643 seasonal and inter-annual variations in the forcing. The cyclonic circulation and the eastern boundary
644 current towards the north in the upper layer is stronger in autumn and winter, as noted by previous
645 simulations (Jędrasik & Kowalewski, 2019), when strong southwesterly winds are more frequent
646 (Soomere & Keevallik, 2001). Quasi-steady circulation patterns were characterized by complicated
647 lateral vortices with the zonal scale of 20–60 km. The richness of vortical structures has been suggested
648 by several numerical modeling studies (Dargahi, 2019; Zhurbas et al., 2021). In-situ measurements are
649 needed to verify the existence of the vortices and to characterize their effect on the physical and
650 biogeochemical fields in more detail.

651 Two quasi-permanent circulation features were detected in the deep layer. Cyclonic gyre was present
652 below the halocline in the Eastern Gotland Basin, with the strongest flow along the eastern slope, which
653 has been documented by in-situ measurements earlier (Hagen & Feistel, 2004; Hagen & Feistel, 2007).
654 The northern branch of the Eastern Gotland Basin current is connected to the quasi-steady northward-
655 flowing current towards narrow Fårö sill between the Fårö and Nothern Deep. The width of the current
656 was mostly 10–30 km, but only 5 km at the sill. The mean northward component of the current was 10
657 cm s^{-1}, which can be explained by the mean density structure (Fig. 15a) and is typical for the gravity
658 current in a channel (Zhurbas et al., 2012). This current is an important deeper limb of the Baltic haline
659 conveyor belt (Döös et al., 2004). The current was stronger in the case of northerly winds and weaker
660 during southwesterly wind prevailing. This is typical behavior of the estuarine circulation: up-estuary
661 wind causes weakening or reversal of the deep layer current and down-estuary wind intensification of
662 the estuarine current (Geyer & MacCready, 2014) as observed in the Gulf of Finland (Liblik et al.,
663 2013; Lilover et al., 2017; Suhhova et al., 2018) and several other estuaries (e.g. Giddings &
664 MacCready, 2017; Scully, 2016). In the case of northerly wind, the vertical and horizontal density
665 gradient in the Fårö sill was much stronger (Fig. 15b) than the mean gradient in 2010–2020 (Fig. 15a)
666 according to the simulation. Note that on the right-hand flank, the isopycnals are vertical (Fig. 15b). A
667 similar structure of the gravity current has been measured by acoustic profiling in the Western Baltic
668 (Umlauf et al., 2009). The current to the north and potentially the deep layer water renewal in the
669 Northern Baltic Proper is more intense in March–May when southwesterly winds are less frequent, and
670 the current is weakest in November–December. If the water that overflows the Fårö sill is dense
671 enough, it occupies the Northern Deep bottom layers, and the old, oxygen-depleted bottom water is
672 lifted and advected to the Gulf of Finland, as observed during high Major Baltic Inflow activity (Liblik
673 et al., 2018). If the overflow has a lower density compared to the deep layer waters in the Northern
674 Deep, it does not dive to the bottom but stays as a buoyant layer.

675

676 The most favorable wind for the up-estuary deep layer advection in the Gulf of Finland is from the
677 northeast (Elken et al., 2003). Thus, northerly winds support deep water renewal and strengthening of
678 the stratification all the way from the Gotland Deep to the Gulf of Finland. The deep layer currents are
679 quite well covered by observations in the Gulf of Finland (Lilover et al., 2017; Rasmus et al., 2015;
680 Suhhova et al., 2018). However, observations are lacking from the Gotland Deep to the entrance of the
681 Gulf of Finland. The only in-situ record about the feature between Gotland and Northern Deep is the
682 Argo float track. The Argo trajectory supported our suggestion about the existence of the sub-halocline
683 current to the north. Our simulations suggested that the strength and position of the current did depend
684 on the wind forcing. Observations and simulation results at the channel-like topographic constriction,
685 Slupsk Furrow, in the southern Baltic have shown that the meandering of the gravity current is strongly
686 affected by the bottom topography and wind-forcing (Zhurbas et al., 2012). ADCP measurements are
687 needed to understand the behavior of the sub-halocline current better.

688 Overall, simulated currents quite well agree with the ADCP measurements in the upper layer. However,
689 the meridional component of the simulated current (V_{GETM}) was biased (Fig. 5a). The mean V_{ADCP} was
690 1.1 cm s^{-1}, but the mean V_{GETM} was –3.2 cm s^{-1} at 10 m depth during the study period. Such bias could
691 not be found in the deep layer. Flow to the north was often weaker compared to measurements (V_{ADCP}),
692 and flow to the south was stronger than observed by the ADCP in the upper layer. A similar tendency
693 can be found in a comparison of the ADCP measurements and simulation results in the Gulf of Finland
694 (Suhhova et al., 2015). Near the right-hand side coast (looking up-estuary, i.e., to the east in the Gulf
695 of Finland), the down-estuary flow was stronger and more frequent in the simulation compared to the
696 measurements (see their Fig. 2). Interestingly, a similar bias was detected in the deep layer at the eastern
697 flank of the Gotland Deep at 204 m depth (Placke et al., 2018). Four different models considerably
698 underestimated (Placke et al., 2018) the mean flow to the north derived from observations (Hagen &
699 Feistel, 2004). The first possible explanation for the bias could be the smaller width of the boundary
700 current. Indeed, the mean flow towards north in 2010–2020 was stronger in the east from the ADCP
701 location (Fig. 12). The second possible source for the discrepancy could be related to the performance
702 of simulation of ageostrophic or geostrophic flow. We will discuss this further in the next section.

703 Quite large discrepancies between the simulation and the measurements occurred in June. In the first
704 half of the month, simulation was biased to the south, but in the second half, a bias to the north can be
705 seen (Fig. 5a). In both cases, the geostrophic current seems to play an important role in the discrepancy.
706 Strong simulated $V_{GEO-DENS-GETM}$ to the south (north) occurred in the first (second) part of June. In
707 August, the simulation did not capture the strongest flow event to the north on 21–24 August (Fig. 5a).
708 At the same period, much lower values of the $V_{GEO-DENS-GETM}$ compared to the $V_{GEO-DENS-glider}$ can be
709 seen. These signs suggest, first, that the isopycnals in the model react to the forcing more rapidly than
710 in the sea. Secondly, there is a bias in the across/slope seasonal thermocline inclination. Likely, the
711 thermocline is tilted more towards the surface near the coast in the model than in the sea. We next
712 evaluate the measured (by glider) and simulated temperature, salinity and geostrophic velocity fields
713 on 11–12 August and on 22–23 August.

714 Surface layer geostrophic velocity in the simulation agrees well with the estimates from the glider data
715 on 11–12 August (Fig. 16a–b). Though, the glider observations reveal sharper thermocline inclination
716 than the simulation. Discrepancies in the temperature, density, and geostrophic current fields on 22–
717 23 August are much larger (Fig. 16c–d). Glider observations revealed the thermocline depressed down
718 near the coast, which is typical for a downwelling. The inclination in the thermocline caused strong
719 geostrophic flow to the north in the location of ADCP (Fig. 16c). Homogenous mixed layer reached
720 down to 22 m depth at the easternmost end of the section. Such an inclination, well defined
721 homogenous layer and geostrophic current to the north at the ADCP location was not revealed by the
722 simulation (Fig. 16c). Thus, we can conclude that the bias in the boundary current simulation could be
723 related to the inaccuracy of reproducing the temperature and salinity fields and the resulting
724 geostrophic component of currents. We are not going into further details of this problem here, as it is
725 out of the focus of the present work. However, conclusions of the simulation studies that have focused
726 on the long-term mean current fields in the upper layer, but did not validate simulations with direct
727 current observations, should be taken carefully, as the magnitude of the long-term residual current is
728 very small compared to the magnitude of the currents during the quasi-steady states. We suggest a
729 dedicated study involving numerous current profiling records should be conducted to track down the
730 causes of the discrepancies between observations and simulations.

731
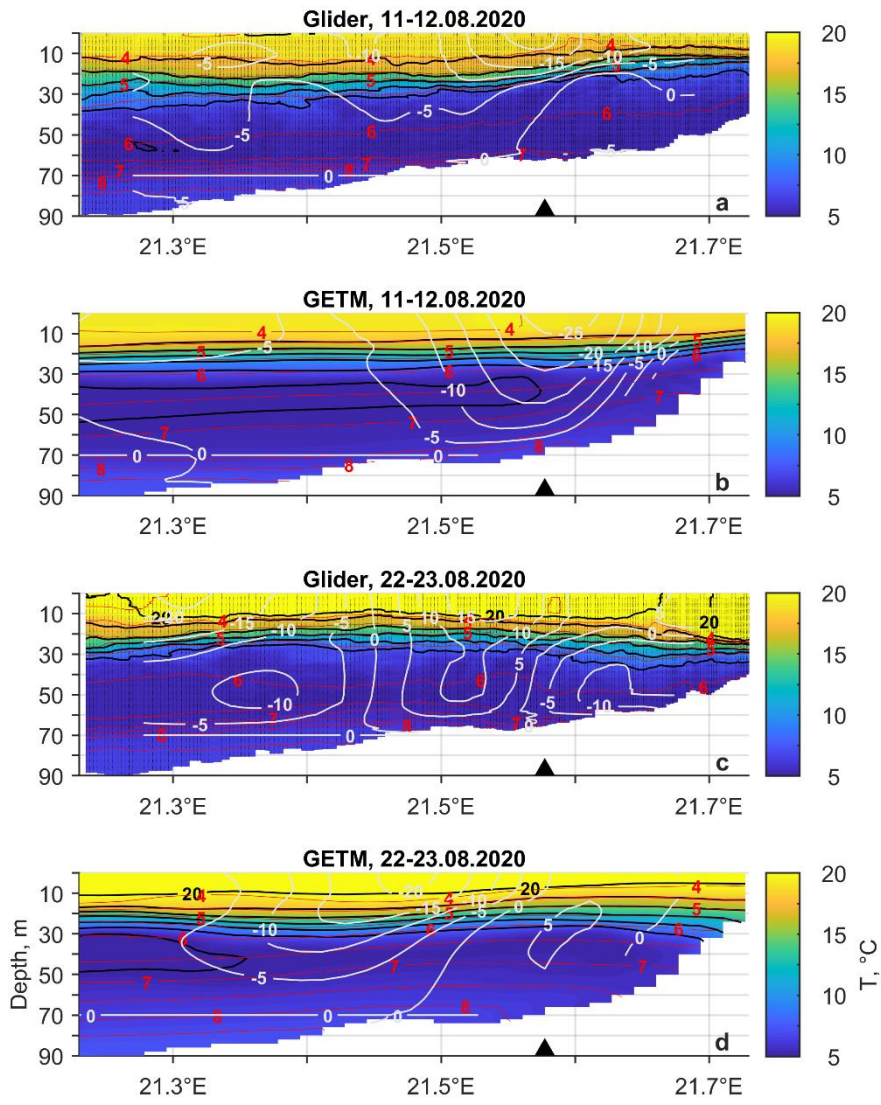
Figure 16. Temperature (color contours), density isolines (red lines), relative geostrophic current (white lines) based on glider observations and GETM simulation on 11–12 August and 22–23 August 2020.

5 Conclusions

A strong link between the existence and location of the two pycnoclines and the current structure was observed. Boundary current was observed in the upper layer along the eastern coast of the Baltic Proper. The current was mainly in geostrophic balance, ~~but~~and across-shore Ekman transport created preconditions for the geostrophic coastal current. The boundary current rapidly reacted to the changes in the wind forcing that was~~is~~ reflected in a relatively low persistency of currents (30–40%) in the whole water column during the 6-month measurement period. However, the quasi-steady circulation patterns formed under the certain wind and stratification conditions were high-persistent (mostly >80%) and generally in the geostrophic balance.

The sub-halocline, quasi-steady northward (towards Fårö sill) gravity current with a width of 10–30 km was detected by the simulation. The finding was supported by the Argo float displacement data. This important deeper limb of the Baltic Sea haline conveyor belt was~~is~~ stronger in the case of northerly winds and weaker during south-westerlies. More detailed studies of the dynamics and water properties of this current are essential to understand the renewal process of deep layer waters in the Northern Baltic Proper and in the Gulf of Finland.

Generally, the structure of boundary current was well reproduced by the GETM. However, the meridional component of the simulated current was biased southward. Further *in-situ* measurements and simulations ~~investigations~~ of the current regimes in various locations during the periods of quasi-steady forcing could help to reveal the causes of the discrepancy.

776

777

References

779 Berden, G., Charo, M., Möller, O. O., & Piola, A. R. (2020). Circulation and Hydrography in the
780   Western South Atlantic Shelf and Export to the Deep Adjacent Ocean: 30°S to 40°S. *Journal of*
781   *Geophysical Research: Oceans*, *125*(10), e2020JC016500.
782   https://doi.org/10.1029/2020JC016500

783 Book, J., Perkins, H., Signell, R., & Wimbush, M. (2007). The Adriatic Circulation Experiment
784   winter 2002/2003 mooring data report: a case study in ADCP data processing. In *U.S. Naval*
785   *Res. Lab. Stennis Space Center*.

786 Burchard, H., & Bolding, K. (2002). *GETM – a general estuarine transport model. Scientific*
787   *Documentation. Technical report EUR 20253 en. In: Tech. Rep. European Commission*.

788 Carstensen, J., Andersen, J. H., Gustafsson, B. G., & Conley, D. J. (2014). Deoxygenation of the
789   baltic sea during the last century. *Proceedings of the National Academy of Sciences of the*
790   *United States of America*, *111*(15), 5628–5633. https://doi.org/10.1073/pnas.1323156111

791 Csanady, G. T. (1981). Circulation in the Coastal Ocean. *Advances in Geophysics*, *23*(C), 101–183.
792   https://doi.org/10.1016/S0065-2687(08)60331-3

793 Dargahi, B. (2019). Dynamics of vortical structures in the Baltic Sea. *Dynamics of Atmospheres and*
794   *Oceans*, *88*, 101117. https://doi.org/10.1016/j.dynatmoce.2019.101117

795 Davis, R. E. (2010). On the coastal-upwelling overturning cell. *Journal of Marine Research*, *68*(3–4),
796   369–385. https://doi.org/10.1357/002224010794657173

797 Döös, K., Meier, H. E. M., & Döscher, R. (2004). The Baltic Haline Conveyor Belt or The
798   Overturning Circulation and Mixing in the Baltic. *AMBIO: A Journal of the Human*
799   *Environment*, *33*(4), 261–266. https://doi.org/10.1579/0044-7447-33.4.261

800 Ekman, V. W. (1905). On the influence of the earth's rotation on ocean currents. *Arkiv. Mat., Astron.*
801   *Fys.*, *11*, 1–52.

802 Elken, J., Raudsepp, U., & Lips, U. (2003). On the estuarine transport reversal in deep layers of the
803   Gulf of Finland. *Journal of Sea Research*, *49*(4), 267–274. https://doi.org/10.1016/S1385-
804   1101(03)00018-2

805 Geyer, W. R., & MacCready, P. (2014). The Estuarine Circulation. *Annual Review of Fluid*
806   *Mechanics*, *46*(1), 175–197. https://doi.org/10.1146/annurev-fluid-010313-141302

807 Giddings, S. N., & MacCready, P. (2017). Reverse Estuarine Circulation Due to Local and Remote
808   Wind Forcing, Enhanced by the Presence of Along-Coast Estuaries. *Journal of Geophysical*
809   *Research: Oceans*, *122*(12), 10184–10205. https://doi.org/10.1002/2016JC012479

810 Gilcoto, M., Largier, J. L., Barton, E. D., Piedracoba, S., Torres, R., Graña, R., Alonso-Pérez, F.,
811   Villacieros-Robineau, N., & de la Granda, F. (2017). Rapid response to coastal upwelling in a

semienclosed bay. *Geophysical Research Letters*, *44*(5), 2388–2397.
https://doi.org/10.1002/2016GL072416

Golenko, M., Krayushkin, E., & Lavrova, O. (2017). Современные проблемы дистанционного зондирования Земли из космоса. *Current Problems in Remote Sensing of the Earth from Space.*, 280–296. https://doi.org/10.21046/2070-7401-2017-14-7-280-296

Hagen, E., & Feistel, R. (2004). Observations of low-frequency current fluctuations in deep water of the Eastern Gotland Basin/Baltic Sea. *Journal of Geophysical Research: Oceans*, *109*(C3). https://doi.org/10.1029/2003JC002017

Hagen, Eberhard, & Feistel, R. (2007). Synoptic changes in the deep rim current during stagnant hydrographic conditions in the Eastern Gotland Basin, Baltic Sea. *Oceanologia*, *49*(2), 185–208.

Hersbach, H., Bell, B., Berrisford, P., Hirahara, S., Horányi, A., Muñoz-Sabater, J., Nicolas, J., Peubey, C., Radu, R., Schepers, D., Simmons, A., Soci, C., Abdalla, S., Abellan, X., Balsamo, G., Bechtold, P., Biavati, G., Bidlot, J., Bonavita, M., … Thépaut, J.-N. (2020). The ERA5 global reanalysis. *Quarterly Journal of the Royal Meteorological Society*, *146*(730), 1999–2049. https://doi.org/10.1002/QJ.3803

Hinrichsen, H. H., von Dewitz, B., & Dierking, J. (2018). Variability of advective connectivity in the Baltic Sea. *Journal of Marine Systems*, *186*, 115–122. https://doi.org/10.1016/j.jmarsys.2018.06.010

Holtermann, P. L., Prien, R., Naumann, M., Mohrholz, V., & Umlauf, L. (2017). Deepwater dynamics and mixing processes during a major inflow event in the central Baltic Sea. *Journal of Geophysical Research: Oceans*, *122*(8), 6648–6667. https://doi.org/10.1002/2017JC013050

Jakobsen, F., Hansen, I. S., Ottesen Hansen, N. E., & Østrup-Rasmussen, F. (2010). Flow resistance in the Great Belt, the biggest strait between the North Sea and the Baltic Sea. *Estuarine, Coastal and Shelf Science*, *87*(2), 325–332. https://doi.org/10.1016/j.ecss.2010.01.014

Janssen, F., Schrum, C., & Backhaus, J. O. (1999). A climatological data set of temperature and salinity for the Baltic Sea and the North Sea. *Deutsche Hydrographische Zeitschrift*, *51*(S9), 5–245. https://doi.org/10.1007/BF02933676

Jedrasik, J., Cieślikiewicz, W., Kowalewski, M., Bradtke, K., & Jankowski, A. (2008). 44 Years Hindcast of the sea level and circulation in the Baltic Sea. *Coastal Engineering*, *55*(11), 849–860. https://doi.org/10.1016/j.coastaleng.2008.02.026

Jędrasik, J., & Kowalewski, M. (2019). Mean annual and seasonal circulation patterns and long-term variability of currents in the Baltic Sea. *Journal of Marine Systems*, *193*, 1–26. https://doi.org/10.1016/j.jmarsys.2018.12.011

Jönsson, B., Döös, K., Nycander, J., & Lundberg, P. (2008). Standing waves in the Gulf of Finland and their relationship to the basin-wide Baltic seiches. *Journal of Geophysical Research*, *113*(C3), C03004. https://doi.org/10.1029/2006JC003862

Krayushkin, E., Lavrova, O., & Strochkov, A. (2019). Application of GPS/GSM Lagrangian mini-drifters for coastal ocean dynamics analysis. *Russian Journal of Earth Sciences*, *19*(1).

850   https://doi.org/10.2205/2018ES000642

Leppäranta, M., & Myrberg, K. (2009). Circulation. In *Physical Oceanography of the Baltic Sea* (pp. 131–187). Springer Berlin Heidelberg. https://doi.org/10.1007/978-3-540-79703-6_5

Liblik, T., Laanemets, J., Raudsepp, U., Elken, J., & Suhhova, I. (2013). Estuarine circulation reversals and related rapid changes in winter near-bottom oxygen conditions in the Gulf of Finland, Baltic Sea. *Ocean Science*, *9*, 917–930.

Liblik, T., Naumann, M., Alenius, P., Hansson, M., Lips, U., Nausch, G., Tuomi, L., Wesslander, K., Laanemets, J., & Viktorsson, L. (2018). Propagation of Impact of the Recent Major Baltic Inflows From the Eastern Gotland Basin to the Gulf of Finland. *Frontiers in Marine Science*, *5*, 222. https://doi.org/10.3389/fmars.2018.00222

Liblik, T., Väli, G., Lips, I., Lilover, M.-J., Kikas, V., & Laanemets, J. (2020). The winter stratification phenomenon and its consequences in the Gulf of Finland, Baltic Sea. *Ocean Science*, *16*, 1475–1490.

Lilover, M.-J., Elken, J., Suhhova, I., & Liblik, T. (2017). Observed flow variability along the thalweg, and on the coastal slopesof the Gulf of Finland, Baltic Sea. *Estuarine, Coastal and Shelf Science*, *195*, 23–33.

Lilover, M.-J., Pavelson, J., & Kõuts, T. (2011). Wind forced currents over the shallow naissaar Bank in the Gulf of Finland. In *Boreal environment research* (Vol. 16).

Longdill, P. C., Healy, T. R., & Black, K. P. (2008). Transient wind-driven coastal upwelling on a shelf with varying width and orientation. *New Zealand Journal of Marine and Freshwater Research*, *42*(2), 181–196. https://doi.org/10.1080/00288330809509947

Macdonald, A. M. (1998). The global ocean circulation: a hydrographic estimate and regional analysis. *Progress in Oceanography*, *41*(3), 281–382. https://doi.org/10.1016/S0079-6611(98)00020-2

Matthäus, W., & Franck, H. (1992). Characteristics of major Baltic inflows—a statistical analysis. *Continental Shelf Research*, *12*(12), 1375–1400. https://doi.org/doi:10.1016/0278-4343(92)90060-W

McDougall, T. J., & Barker, P. M. (2011). Getting started with TEOS-10 and the Gibbs Seawater (GSW) Oceanographic Toolbox. *SCOR/IAPSO WG127*, 28pp. https://doi.org/ISBN 978-0-646-55621-5

Meier, H. E. . (2007). Modeling the pathways and ages of inflowing salt- and freshwater in the Baltic Sea. *Estuarine, Coastal and Shelf Science*, *74*(4), 610–627. https://doi.org/10.1016/J.ECSS.2007.05.019

Mohrholz, V. (2018). Major Baltic Inflow Statistics – Revised. *Frontiers in Marine Science*, *5*, 384. https://doi.org/10.3389/fmars.2018.00384

Ollitrault, M., & Rannou, J.-P. (2013). *ANDRO: An Argo-based deep displacement dataset*. https://doi.org/http://doi.org/10.17882/47077

887 Placke, M., Meier, H. E. M., Gräwe, U., Neumann, T., Frauen, C., & Liu, Y. (2018). Long-Term
888   Mean Circulation of the Baltic Sea as Represented by Various Ocean Circulation Models.
889   *Frontiers in Marine Science*, *5*(SEP), 287. https://doi.org/10.3389/fmars.2018.00287

890 Rasmus, K., Kiirikki, M., & Lindfors, A. (2015). Long-term field measurements of turbidity and
891   current speed in the Gulf of Finland leading to an estimate of natural resuspension of bottom
892   sediment. *Boreal Environment Research* , *20*, 735–747.
893   http://www.borenv.net/BER/pdfs/ber20/ber20-735.pdf

894 Reissmann, J. H., Burchard, H., Feistel, R., Hagen, E., Lass, H. U., Mohrholz, V., Nausch, G.,
895   Umlauf, L., & Wieczorek, G. (2009). Vertical mixing in the Baltic Sea and consequences for
896   eutrophication - A review. In *Progress in Oceanography* (Vol. 82, Issue 1, pp. 47–80).
897   https://doi.org/10.1016/j.pocean.2007.10.004

898 Rubio, A., Gomis, D., Jordà, G., Espino, M., Rubio, A., Gomis, D., Jordà, G., & Espino, M. (2009).
899   Estimating geostrophic and total velocities from CTD and ADCP data: Intercomparison of
900   different methods. *JMS*, *77*(1), 61–76. https://doi.org/10.1016/J.JMARSYS.2008.11.009

901 Scully, M. E. (2016). Mixing of dissolved oxygen in Chesapeake Bay driven by the interaction
902   between wind-driven circulation and estuarine bathymetry. *Journal of Geophysical Research:
903   Oceans*, *121*(8), 5639–5654. https://doi.org/10.1002/2016JC011924

904 Siiriä, S., Roiha, P., Tuomi, L., Purokoski, T., Haavisto, N., & Alenius, P. (2019). Applying area-
905   locked, shallow water Argo floats in Baltic Sea monitoring. *Journal of Operational
906   Oceanography*, *12*(1), 58–72. https://doi.org/10.1080/1755876X.2018.1544783

907 Sokolov, A., & Chubarenko, B. (2012). Wind Influence on the Formation of Nearshore Currents in
908   the Southern Baltic: Numerical Modelling Results. *Archives of Hydroengineering and
909   Environmental Mechanics*, *59*(1–2), 37–48. https://doi.org/10.2478/v10203-012-0003-3

910 Soomere, T., & Keevallik, S. (2001). Anisotropy of moderate and strong winds in the Baltic Proper.
911   In *Proc. Estonian Acad. Sci. Eng* (Vol. 7, Issue 1). http://kirj.ee/public/va_te/t50-1-3.pdf

912 Suhhova, I., Liblik, T., Lilover, M.-J., & Lips, U. (2018). A descriptive analysis of the linkage
913   between the vertical stratification and current oscillations in the Gulf of Finland. *Boreal
914   Environment Researchesearch*, *23*, 83–103.

915 Suhhova, I., Pavelson, J., & Lagemaa, P. (2015). Variability of currents over the southern slope of
916   the Gulf of Finland. *Oceanologia*, *57*(2), 132–143. https://doi.org/10.1016/j.oceano.2015.01.001

917 Umlauf, L., Arneborg, L., Umlauf, L., & Arneborg, L. (2009). Dynamics of Rotating Shallow
918   Gravity Currents Passing through a Channel. Part I: Observation of Transverse Structure.
919   *Journal of Physical Oceanography*, *39*(10), 2385–2401. https://doi.org/10.1175/2009JPO4159.1

920 Umlauf, L., & Burchard, H. (2005). Second-order turbulence closure models for geophysical
921   boundary layers. A review of recent work. *Continental Shelf Research*, *25*, 795–827.
922   https://doi.org/10.1016/j.csr.2004.08.004

923 Väli, G., Meier, H. E. M., & Elken, J. (2013). Simulated halocline variability in the Baltic Sea and its
924   impact on hypoxia during 1961-2007. *Journal of Geophysical Research: Oceans*, *118*(12),

925   6982–7000. https://doi.org/10.1002/2013JC009192

926   Villacieros-Robineau, N., Herrera, J. L., Castro, C. G., Piedracoba, S., & Roson, G. (2013).
927   Hydrodynamic characterization of the bottom boundary layer in a coastal upwelling system (Ría
928   de Vigo, NW Spain). *Continental Shelf Research*, *68*, 67–79.
929   https://doi.org/10.1016/j.csr.2013.08.017

930   Wu, H., Deng, B., Yuan, R., Hu, J., Gu, J., Shen, F., Zhu, J., Zhang, J., Wu, H., Deng, B., Yuan, R.,
931   Hu, J., Gu, J., Shen, F., Zhu, J., & Zhang, J. (2013). Detiding Measurement on Transport of the
932   Changjiang-Derived Buoyant Coastal Current. *Journal of Physical Oceanography*, *43*(11),
933   2388–2399. https://doi.org/10.1175/JPO-D-12-0158.1

934   Wu, J. (1980). Wind-Stress coefficients over Sea surface near Neutral Conditions—A Revisit.
935   *Journal of Physical Oceanography*, *10*(5), 727–740. https://doi.org/10.1175/1520-
936   0485(1980)0102.0.co;2

937   Zhurbas, V., Elken, J., Paka, V., Piechura, J., Väli, G., Chubarenko, I., Golenko, N., & Shchuka, S.
938   (2012). Structure of unsteady overflow in the supsk furrow of the baltic sea. *Journal of
939   Geophysical Research: Oceans*, *117*(4), 4027. https://doi.org/10.1029/2011JC007284

940   Zhurbas, V., Väli, G., Golenko, M., & Paka, V. (2018). Variability of bottom friction velocity along
941   the inflow water pathway in the Baltic Sea. *Journal of Marine Systems*, *184*, 50–58.
942   https://doi.org/10.1016/J.JMARSYS.2018.04.008

943   Zhurbas, V., Väli, G., & Kuzmina, N. (2021). Striped texture of submesoscale fields in the
944   northeastern Baltic Proper: Results of very high-resolution modelling for summer season.
945   *Oceanologia*. https://doi.org/10.1016/J.OCEANO.2021.08.003

946